DESIGN AND ANALYSIS OF METAMATERIAL BASED PERFECT ABSORBERS

A THESIS SUBMITTED TO
THE GRADUATE SCHOOL OF ENGINEERING AND SCIENCE
OF BILKENT UNIVERSITY
IN PARTIAL FULFILLMENT OF THE REQUIREMENTS FOR
THE DEGREE OF
MASTER OF SCIENCE
IN
ELECTRICAL AND ELECTRONICS ENGINEERING

By
Mahmut Can Soydan
August 2019

DESIGN AND ANALYSIS OF METAMATERIAL BASED PERFECT ABSORBERS

By Mahmut Can Soydan

August 2019

We certify that we have read this thesis and that in our opinion it is fully adequate, in scope and in quality, as a thesis for the degree of Master of Science.

Vakur Behçet Ertürk(Advisor)

Ekmel Özbay(Co-Advisor)

Ergin Atalar

İbrahim Tuna Özdür

Approved for the Graduate School of Engineering and Science:

Ezhan Karaşan
Director of the Graduate School

ABSTRACT

DESIGN AND ANALYSIS OF METAMATERIAL BASED PERFECT ABSORBERS

Mahmut Can Soydan
M.S. in Electrical and Electronics Engineering
Advisor: Vakur Behçet Ertürk
Co-Advisor: Ekmel Özbay
August 2019

Subwavelength light absorbers have an enormous potential on applications such as photodetection, optoelectronics, solar cells and sensing. Scaling down the device dimensions provides artificial and advanced properties. That's why achieving higher performance devices with smaller sizes is the main trend in semiconductor technology. Design of an electromagnetic wave absorber has two dominant factors on the performance and spectral operation region: material selection and design configuration. Perfect light absorbers require an absorbing layer, such as a metal, semiconductor or any type of absorbing material, to achieve light confinement. While conventional metals have been mostly the primary choice in designs, there are various material types other than them which can have advantageous thermal properties in fabrication, integration or tunability besides having lossy nature.

Although conventional metals are great absorbing materials due to lossy natures, they are not durable against erosion and oxidation. In the first work, we scrutinize unprecedented potential of transition metal carbides (TMCs) and nitrides (TMNs) as optional materials to conventional metals, for realization of light perfect absorption in an ultra-broad frequency range encompassing all of the visible (Vis) and near infrared (NIR) regions. To gain insight on the condition for light perfect absorption, a systematic modeling approach based on transfer matrix method (TMM) is firstly utilized. Our modeling findings prove that the permittivity data of these TMCs and TMNs are closely matched with the ideal data. Thus, they can have stronger and broader absorption behavior compared to metals. Besides, these ceramic materials are preferred to metals due to the fact that they have better thermal properties and higher durability against erosion and oxidation than metals. This could provide the opportunity for design of highly efficient light harvesting systems with long-term stability. Two different

configurations which are planar and trapezoidal arrays are employed. Numerical simulations are conducted to optimize the device optical performance for each of the proposed carbides and nitrides. Our findings reveal that these ceramic coatings have the broadest absorption response compared to all lossy and plasmonic metals. In planar configuration, titanium carbide (TiC) has the largest absorption bandwidth (BW) where an absorption above 0.9 is retained over a broad wavelength range of 405 nm-1495 nm. In trapezoid architecture, vanadium nitride (VN) shows the widest BW covering a range from 300 nm to 2500 nm. The results of this study can serve as a beacon for the design of future high performance energy conversion devices including solar vapor generation and thermal photovoltaics where both optical and thermal requirements can be satisfied.

Majority of existing designs necessitate a lithography-step during the fabrication, which hinders the repeatability, upscaling and large-scale compatibility of these designs. In the second work, we designed, fabricated and characterized a lithography free, double functional single Bismuth (Bi) metal nanostructure for ultra-broadband absorption in the visible and near-infrared, and narrowband response with ultra-high refractive-index sensitivity in mid-infrared (MIR) range. The superior permittivity data of Bi over conventional metals is comprehensively analyzed and explained using systematic modeling approaches based on TMM and Bruggeman's effective medium theory (EMT). To achieve a large scale fabrication of the design in a lithography-free route, oblique-angle deposition approach is used to obtain densely packed and randomly spaced/oriented Bi nanostructures. It has been shown that this fabrication technique can provide a bottom-up approach to control the length and spacing of the design. Our characterization findings reveal a broadband absorption above 0.8 in Vis and NIR, and a narrowband absorption centered around 6.54 μm. Due to densely packed architecture of the Bi nanostructures and its extraordinary permittivity response, they can provide strong field confinement in their ultra-small gaps and this could be utilized for sensing application. An ultrahigh sensitivity of 2.151 μm/refractive-index-unit (RIU) is acquired for this Bi nanostructured absorber, which is, to the best of our knowledge, the experimentally attained highest sensitivity so far. The simple and large scale compatible fabrication route of the design together with extraordinary optical response of Bi coating, makes this design promising for many optoelectronic and sensing applications.

Keywords: perfect absorbers, broadband, narrowband, sensor, metamaterial.

ÖZET

METAMALZEME BAZLI MÜKEMMEL SOĞURUCULARIN DİZAYN VE ANALİZİ

Mahmut Can Soydan
Elektrik ve Elektronik Mühendisliği, Yüksek Lisans
Tez Danışmanı: Vakur Behçet Ertürk
İkinci Tez Danışmanı: Ekmel Özbay
Ağustos 2019

Dalga boyundan daha küçük boyuttaki ışık soğurucuları optoelektronik, foton algılama, solar hücre ve sensör alanlarında çok büyük bir potansiyele sahiptir. Cihazın boyutlarını küçültmek yapay ve ileri seviye özellikler kazandırır. Günümüz yarı iletken teknolojisindeki daha küçük boyutta ve daha yüksek performans gösteren cihazların üretilmeye çalışılmasının yükselen bir trend olması bundan dolayıdır. Elektromanyetik dalga soğurucularının performansını ve çalıştığı ışık tayfı bölgesini belirleyen iki temel özellik vardır: malzeme seçimi ve yapının şekli. Mükemmel ışık soğurucuları ışığı yapılarında hapsedebilmek için bir metal, yarı iletken veya herhangi çeşitte soğurma özelliği olan bir katmana ihtiyaç duyar. Geleneksel metaller çoğunlukla birincil olarak tercih edilen malzeme olmasına rağmen hem yitimli bir yapıya sahip olan hem de üretim, entegrasyon ve ayarlanabilirlik gibi daha üstün termal özellikleri olan başka türde malzemeler de mevcuttur.

Geleneksel metaller yitimli bir yapıya sahip olmaları sebebiyle harika soğrucu malzemeler olmalarına rağmen aşınma ve oksitlenmeye karşı dayanıklı değillerdir. İlk çalışmamızda, geleneksel metallere alternatif bir malzeme olarak geçiş metali karbürlerinin ve geçiş metali nitrürlerinin ışığın görünür bölgeden (Vis) yakın kızıl ötesi bölgeye (NIR) kadar çok geniş bir frekans aralığında mükemmel bir şekilde soğurulmasındaki eşsiz potansiyelini inceledik. İlk olarak, mükemmel ışık soğurucularının gereksinimleri hakkında bir öngörü sahibi olmak için geçiş matrisi metodu (TMM) olarak adlandırılan sistematik bir modelleme tekniği kullanıldı. Elde edilen modelleme sonuçları geçiş metali karbürlerinin ve nitrürlerinin elektriksel geçirgenlik değerlerinin ideal değerler ile çok iyi örtüştüğünü ispatlamaktadır. Ayrıca bu seramik malzemeler metallere kıyasla daha iyi termal özelliklere

ve de aşınma ve oksitlenmeye karşı dayanıklı olduklarından da tercih edilmektedirler. Bu özellikleri sayesinde yüksek verimlilikle çalışan ve uzun süreli stabil olan ışık toplayan sistemlerin dizaynı için bir fırsat sunmaktadırlar. Düzlemsel ve ikizkenar yamuk şeklinde sıralanmış katmanlardan oluşan iki farklı şekil kullanıldı. Numerik simülasyon teknikleri kullanılarak her bir karbür ve nitrür için yapıların optik performansları optimize edildi. Bulunan sonuçlar bu seramik malzemelerin bütün yitimli yapıdaki ve plazmonik özellikteki metallere kıyasla daha geniş aralığı soğurabildiğini göstermektedir. Düzlemsel dizilişte titanyum karbür (TiC) 405 nm-1495 nm aralığı kadar geniş bir bandı 0.9'un (normalize olarak) üzerinde soğurarak en geniş soğurma bandını gerçekleştirmiştir. İkizkenar yamuk dizilişinde ise vanadyum nitrürün (VN) 300 nm ile 2500 nm aralığı kadar geniş bir bant genişliğine sahip olduğu görülmüştür. Bu çalışmanın çıktıları solar buhar üretimi ve termal fotovoltaik gibi hem optik hem de termal gereksinimleri olan alanlar dahil olmak üzere gelecekteki yüksek performanslı enerji dönüşüm cihazlarının dizaynı konusunda bir yol ışığı olabilecek niteliktedir.

Mevcut dizaynların büyük bir çoğunluğu üretim aşamasında bir litografi aşaması gerektirmektedir, ki bu da yapının büyük boyutlarda üretilmeye uygunluğunu ve tekrar edilebilirliğini engellemektedir. İkinci çalışmamızda, litografisiz üretilebilen, sadece bizmut (Bi) metalinden yapılmış nanoyapılardan oluşan, çift fonksiyon gösteren, görünür ve yakın kızıl ötesi bölgede çok geniş bantlı soğurucu, orta kızıl ötesi bölgede ise çok yüksek kırıcılık indisi hassaslığı olan bir dart bantlı soğurucu olarak davranan bir yapı dizayn ettik, ürettik ve karakterize ettik. Bizmutun geleneksel metallere kıyasla çok daha iyi bir elektriksel geçirgenlik özelliği olduğu geçiş matrisi metodu ve Bruggeman'ın etkin ortam kuramı (EMT) kullanılarak ayrıntılı bir şekilde incelendi ve açıklandı. Yapının litografi kullanılmadan, büyük boyutlarda üretimini mümkün kılacak şekilde üretilmesi için eğik açılı kaplama tekniği kullanılarak çok yoğun biçimde dizilmiş ve rastgele yerleşmiş/yönelmiş Bi nanoyapıları elde edildi. Ayrıca, bu üretim tekniğinin alttan üste işlemleme yaklaşımıyla üretilen yapının yerleşmesinin ve uzunluğunun kontrol edildiği gösterilmiştir. Karakterizasyon sonuçlarına göre yapı görünür ve yakın kızılötesi bölgelerinde 0.8 üzerinde soğurmaya sahipken orta kızılötesi bölgede ise 6.54 micrometrede (μm) merkezlenmiş dar bantlı bir soğurma göstermektedir. Bi yapılarının çok yoğun bir biçimde paketlenmesinden ve sıradışı bir geçirgenlik özelliğine sahip olmasından dolayı nanoyapılar, aralarındaki çok küçük boşluklarda güçlü bir şekilde ışığı hapsedebilmektedir ve bu özellikleri algılama uygulamalarında kullanılmaya uygundur. Yapılan incelemede

Bi nanoyapılarının 2.151 μm/birim kırıcılık indisi (RIU) kadar yüksek bir hassaslık değerine sahip olduğu ölçülmüştür. Bu değer bilindiği kadarıyla şimdiye kadar deneysel olarak elde edilen en yüksek hassaslık değeridir. Basit ve büyük boyutlarda üretime uygun olan üretim rotasının olması ve bizmutun eşsiz optik özellikleri, bu dizaynı birçok optoelektronik ve sensör uygulamaları için ümit verici kılmaktadır.

Anahtar sözcükler: mükemmel soğurucu, geniş bantlı, dar bantlı, sensör, metamalzeme.

Acknowledgement

First, I would like to express my sincere gratitude and appreciation to Prof. Ekmel Özbay and Prof. Vakur B. Ertürk for their wise supervision and guidance, endless support and understanding, encouragement and being a role model. They became more than supervisor of my master degree, a guide with friendly wishes. Second, I would like to thank to Prof. Ergin Atalar and Assoc. İbrahim T. Tüzün for allocating their valuable time for being a member of my thesis committe and their priceless comments to make this thesis better.

I would like to thank Amir Ghobadi for advising me all the time, for teaching me almost everything I learned both theoretical and practical, for sharing his priceless ideas and comments on my researches and for each second we spent together. He is a very good researcher who has full knowledge of broadband perfect absorbers, and an insightful mentor who contributes to each person worked with him. He is more than a friend for me, like an older brother which will never be forgotten. I also would like to state my gratitude to UNAM and NANOTAM families, especially to Murat Gökbayrak, Ahmet Toprak and Okan Ateşal, for giving training to use fabrication equipment and for fulfilling my requests for projects.

I would like to thank to my office mates, Deniz Umut Yıldırım, Ataollah Kalantari, Salahaddin Zafar, Oğuz Odabaşı, Tayfur Kaya, Hodjat Haijan and Engin Arslan, for the friendly and amusing environment they provided which was perfect for lightening the stress load and having good time while learning. I especially thank to Deniz and Engin for assisting discussions and polite behaviors.

I am also grateful to my friends since from undergraduate education, Erdem Aras, Ömer Arol, Bilal Taşdelen, Ahmet Safa Öztürk, Abdulsamet Dağaşan, Dilan Öztürk, Ecrin Yağız, Rahmetullah Çağıl, Muzaffer Özbey, Batuhan Sütbaş, Muhammed Akbulut, Ahmed Selim Akal, Bahadır Vural, Nihat Demir, Selahattin Harmankaya, Numan Uyar and Furkan Alan, and also to my friends from high-school, Ömür Yaşar Bilgin, Mücahit Özden, İlker Ağca, Görkem Akıncı, Aslan

Yıldırım, Erdem Semih Yıldız and Erdi Kaya for their warm company and for all funny moments we witnessed together. Their priceless friendship will last forever.

I also would like to state my deep gratitude to my lifelong partner Mürşide Koç for always being right beside. Whenever I was full of concerns, I got rid of them thanks to her. She helped me to maintain my motivation till the end.

Last but not least, I would like to dedicate this thesis to the unconditional love and support of my parents Hacer Soydan and İsmail Soydan, and my lovely sister Hande Nur Soydan. I could not succeed any of my academical achievements if they were not always there for me. I have felt their trust and support nearby.

Contents

List of Figures

List of Tables

Chapter 1

Introduction

1.1 Background and Applications of Perfect Absorbers

Metamaterials are a class of advanced materials which have exceptional properties that cannot be observed in nature. Designed inclusions in natural materials creates exotic features such as negative refraction [1, 2, 3], artificial magnetism [4, 5], asymmetric transmission [6, 7], lasing [8, 9], cloak of invisibility [10, 11, 12], and subwavelength light absorption [13]. Designing perfect light absorbers, which are capable of confining almost 100% of the electromagnetic wave by subwavelength geometries, has been an emerging topic in nanophotonics and nanoplasmonics in recent years. High performance light confinement in the structure is achieved utilizing an absorbing layer such as a metal or a semiconductor. The major figures of merit of perfect light absorbers are high performance and flat absorption strength (percentage of absorbed light), bandwidth of the perfect absorption, fabrication route, vertical and lateral dimensions of the structure and polarization insensitivity. Designs which have an easy fabrication route, polarization insensitive absorption characteristic and very thin (i.e., subwavelength) geometry are superior to others. Perfect light absorbers are classified in two categories based

on their spectral coverage: narrowband and broadband absorbers. While the narrowband perfect absorbers are of great use in applications of sensing and color filtering [14, 15, 16, 17, 18, 19, 20, 21], broadband absorbers are of particular interest in applications of thermal photovoltaics and photodetection [22, 23, 24], optoelectronics [25, 26, 27, 28, 29, 30, 31, 32, 33, 34, 35, 36], and photoelectrochemical water splitting [37].

Optoelectronic applications require strong and broadband absorption in dimensions comparable to carrier's diffusion length, and much smaller than the light wavelength. Properly designed perfect absorbers provide optically thick, but electrically thin device for these kinds of applications utilizing nanostructures in subwavelength geometries. Photovoltaic solar cells are the devices that produce electricity as output by using electron-hole pairs generated by incoming light. Acquiring near unity absorption in semiconductor based nanostructured ultra-thin layers is an efficient approach. Photoelectrochemical water splitting is a system that contains a photoanode and photocathode made of semiconductor or metal. Interaction between incoming photon light and photoelectrode design results electron-hole pairs. The generated electrons move toward electrode and creates hydrogen. In these applications, reducing the active layer thickness and carrier's diffusion length, which are provided by nanophotonics based perfect absorbers, is an effective approach to increase efficiency of the system. Filters are made of selective absorption of the electromagnetic spectrum with high efficiency and narrow bandwidth. If the selectively absorbed narrow wavelength range is in Visible region, they are called as color filters. Filtering the incoming light can be attained either with reflection of the narrowband or transmission of it. The rest of the spectrum is absorbed by the subwavelength structure. Narrowband perfect absorbers in various cavity designs are used to achieve color filters. In addition, another important application of narrowband perfect absorbers is sensing. The resonance of the structure at a specific wavelength spectrally shifts when it interacts with a different surrounding environment instead of air. The amount of the shift in resonance wavelength depends on the refractive index of the external medium, and therefore, this can be used to identify the type of the surrounding material. Biosensors are one of the most commonly studied areas of sensing

applications.

Perfect absorption in subwavelength dimensions can be attained utilizing different mechanisms such as Fabry-Perot (FP) cavity resonance, excitation of surface plasmon polariton (SPP) or localized surface plasmon (LSP) resonances. FP resonance depends on the cancellation of upward and downward propagating electromagnetic waves inside a metal-insulator cavity. Spectral position of the resonance wavelength shifts in accordance with the thickness of the cavity and permittivity of the materials. Metal-insulator-metal (MIM), metal-insulator-metal-insulator (MIMI) and multiple metal-insulator (MI) layers are commonly used cavity designs. The bottom metallic layer is chosen thick at least 100 nm to act as a reflecting mirror in order to reflect all of the light back into the cavity. The top metallic layer(s) are sufficiently thin that allows the light to penetrate into the cavity, and the top insulator layer behaves like an anti-reflective coating on the metal. SPP and LSP resonances are excited using the phenomena of diffraction and scattering at the metal/insulator interfaces. To achieve the excitation, nanostructures such as nanorings, nanodiscs and nanopatches, are patterned on the top layer to create a nanopatterned surface which enables diffraction using electron beam lithography (EBL) technique. Although MIM designs with nanopatterned top layer present great absorption and bandwidth, fabrication complexity of the samples due to EBL dependence hinders large scale compatibility and further improvement of these structures.

Absorption spectrum bandwidth and strength of perfect light absorbers are leaded by two dominant factors, which are design configuration and material properties. The design architecture and geometries of the nanostructures determine which absorption mechanism will be active to confine the light inside the structure with full efficiency. In addition, the use of the appropriate material in a proper configuration can provide the desired functionality. Generally speaking, noble metals can provide narrowband absorption in the visible range while the lossy ones show an ultra-broadband absorption. Thus, it is of great importance to understand the ideal permittivity values for a perfect absorber. The perfect absorption, in the visible (Vis) and short near-infrared (NIR) regimes, requires a small negative real part of permittivity. While for longer wavelengths, such as

long NIR and mid-infrared (MIR) spectral regions, the permittivity should have positive values. Thus, an ideal metal should act as a lossless noble metal in the short wavelengths and a lossy dielectric in the longer ones. This requirement cannot be satisfied with any common metal (with large negative real permittivity values in NIR and MIR ranges).

1.2 Thesis Organization

The rest of this thesis includes design and analysis of a metal-free broadband perfect absorber and simultaneous realization of broadband absorption and ultra-high sensitive refractive index sensing. In chapter 2, we present the theoretical analysis methods that we used in our researches. Overall reflection and optical properties of an ideal material for a specific design configuration can be predicted using these methods. Therefore, they are essential to select the ideal material in designs. Two systematic modeling approaches, transfer matrix method (TMM) and Bruggeman's effective medium theory (EMT), are explained in a detail way.

In chapter 3, we explain frequently used simulation tool, fabrication and characterization equipment used in the clean room. Numerical simulations based on finite-difference time-domain (FDTD) method are carried out in the design and optimization process of the structures. The fabrication tools to produce designed structure via numerical simulations, and characterization tools to measure optical properties and optical response of the fabricated samples are introduced. Many physical vapor deposition techniques and characterization methods are explained with operating principles.

In chapter 4, we present a metal-free broadband perfect absorber to be used instead of metals, which suffer from erosion and oxidation. First, TMM is carried out to compare optical properties of transition metal carbides and nitrides with conventional metals. Numerical simulations are employed for each material separately in two different design configurations, in MIMI and 3-pairs trapezoidal

array structure. In addition, possible challenges faced in the fabrication process are considered, and alternative designs are proposed to maintain the same performance even if problems are appeared during fabrication.

In chapter 5, we present lithography free, double functional, bismuth (Bi) metal nanostructures which exhibit ultra-broadband absorption in Vis and NIR, and ultra-high sensitive narrowband response in MIR. First, extraordinary permittivity data of Bi is explained theoretically by conducting TMM and EMT. Second, the proposed lithography-free fabrication route and creation of random nanorods are demonstrated using scanning electron microscope images. Simulation and experimental results of the fabricated sample in Vis, NIR and MIR regimes are presented. Last, the sensitivity of the narrowband response is measured experimentally and an ultrahigh sensitivity is acquired, which is, to the best of our knowledge, the experimentally attained highest sensitivity so far.

In chapter 6, we summarize the proposed designs, findings, and possible future applications and research directions.

Chapter 2

Theoretical Analysis

In this chapter, two systematic modeling approaches to analyze designed structures theoretically are introduced: TMM and EMT. For a single interface between two media, the reflected and transmitted portions of the electromagnetic wave are described by the Fresnel coefficients. When there are multiple layers and interfaces, reflected and transmitted light from an interface once again reflects and transmits from the next one. Repetition of this process for each interface creates infinitely many propagating waves upward and downward inside the layers. TMM is a method used in optics to analyze the total reflected and transmitted portion of the light from a multilayered structure. It is an efficient method to calculate total reflection from a planar and multilayer design. Nanostructures on the top layer bring about additional phenomenon such as diffraction, which creates plasmon resonances to confine light. Therefore, TMM cannot predict the overall reflection from the structure in an exact way.

Bruggeman's EMT is an analytical modeling approach that describes the macroscopic features of composite materials. It is developed to predict effective parameters of an inhomogeneous mixture of composite materials using permittivities and filling fractions of the materials in the mixture. It is impossible to make precise calculations; however, using acceptable approximations derives useful parameters for the composite material as a whole. In overall, this method

replaces the composite materials with one final effective medium whose optical parameters are predicted through some approximations.

2.1 Transfer Matrix Method

TMM is a systematic modeling approach that calculates transfer matrices of electric and magnetic fields for multilayer structures. Applying boundary conditions and solving a bunch of equations result the overall reflection and transmission coefficients of the whole structure. In order to obtain perfect absorption (i.e., low reflection), effective permittivity of the metamaterial must be matched to the that of medium of incidence (i.e., air). To demonstrate how this method is carried out, a general scheme of a multi MI-pair structure, see Figure 2.1, will be analyzed. A thick metallic layer, which is at least 100 nm, is coated to act as a perfect reflecting mirror to eliminate transmission from the structure. Depending on the design specifications, N two-layer lossy medium(X)-insulator(I) pairs can be used to create a perfect absorber. All XI-pairs have the same dimensions and optical properties. The lossy medium can be a semiconductor, a metal or any good absorbing material. The schematic representation shown in Figure 2.1 is called as $\mathrm{MI(XI)^N}$. In this description, M,I and X represents bottom metal layer, insulator and lossy medium, respectively. For example, an MIMI design is created using one XI-pair, where lossy medium is chosen as metal. To give another example, an MIM design contains only lossy medium of the first XI-pair on the bottom metal mirror layer and insulator. The structure does not have to include an exact number of XI-pairs.

The overall reflection from a planar multilayer design can be calculated using TMM if refractive indices of materials and their dimensions are known. Besides, the ideal permittivity (ϵ_{X}) of the lossy medium in order to achieve a reflection below a definite value, such as 0.1, can be investigated through TMM. Let me suppose the structure is bounded with air (whose permittivity is ϵ_{A}) and substrate (whose permittivity is ϵ_{S}), and consider $z = 0$ plane as the interface between air and the top insulator layer. The y component of the magnetic field (H_{y}) is given

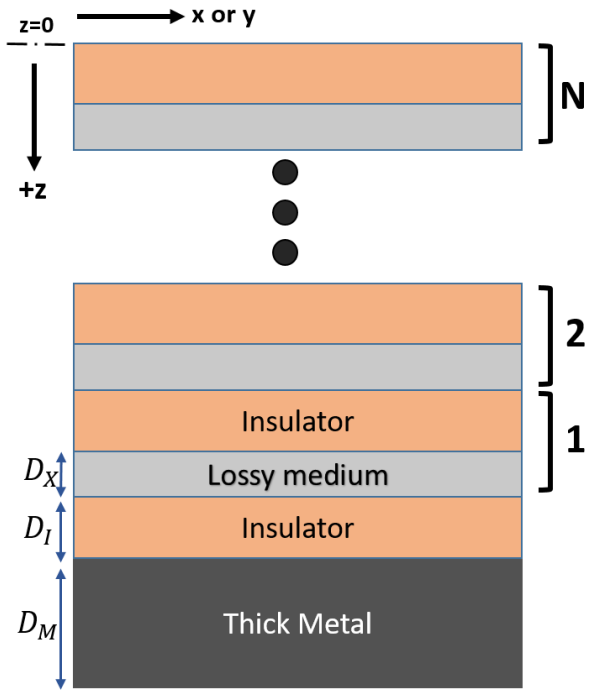

Figure 2.1: Generalized representation of the MI(MI)$^{\mathrm{N}}$ design

by

$$H_y(z) = \begin{cases} A_i e^{ik_A z} + A_r e^{-ik_A z}, & z <= 0 \\ I_{11} e^{ik_I z} + I_{12} e^{-ik_I z}, & 0 < z <= D_I \\ X_{11} e^{ik_X (z-D_I)} + X_{12} e^{-ik_X (z-D_I)}, & D_I < z <= L \\ I_{21} e^{ik_I (z-L)} + I_{22} e^{-ik_I (z-L)}, & L < z <= L + D_I \\ . & \\ . & \\ . & \\ M_{11} e^{ik_M (z-NL-D_I)} + M_{12} e^{-ik_M (z-NL-D_I)}, & NL + D_I < z <= NL + D_I + D_M \\ S_t e^{ik_S [z-(NL+D_I+D_M)]}, & z > NL + D_I + D_M \end{cases} \quad (1)$$

where $L = D_I + D_X$, $k_{j=A,X,I,M,S} = \sqrt{\frac{\epsilon_j \omega^2}{c^2} - k_x^2}$, c is the speed of light, A and S represent air and substrate, and k_x is the wave vector in the x-direction. D_I,

D_X and D_M are the thicknesses of the insulator, lossy and bottom metal layers, respectively. ϵ_j represents the permittivity of different layers. Boundary conditions for transverse magnetic (TM) polarization are solved for the interfaces. TMM results the relation between incident, reflected and transmitted light with the following transfer matrix equation:

$$\begin{bmatrix} A_i \\ A_r \end{bmatrix} = \begin{bmatrix} F_{11} \\ F_{12} \end{bmatrix} S_t \tag{2}$$

Reflection of the incident light from the structure is found as $R = |\frac{F_{11}}{F_{12}}|^2$ using equation 2. Here, $F = \begin{bmatrix} F_{11} \\ F_{12} \end{bmatrix} = A^{-1}(I_1 I_2^{-1} X_1 X_2^{-1})^N I_1 I_2^{-1} M_1 M_2^{-1} S$ where

$$A = \begin{bmatrix} 1 & 1 \\ \frac{ik_A}{\epsilon_A} & \frac{-ik_A}{\epsilon_A} \end{bmatrix}, S = \begin{bmatrix} 1 \\ \frac{ik_S}{\epsilon_S} \end{bmatrix} \tag{3.a}$$

$$I_1 = \begin{bmatrix} 1 & 1 \\ \frac{ik_I}{\epsilon_I} & \frac{-ik_I}{\epsilon_I} \end{bmatrix}, I_2 = \begin{bmatrix} e^{ik_I D_I} & e^{-ik_I D_I} \\ \frac{ik_I e^{ik_I D_I}}{\epsilon_I} & \frac{-ik_I e^{-ik_I D_I}}{\epsilon_I} \end{bmatrix} \tag{3.b}$$

$$X_1 = \begin{bmatrix} 1 & 1 \\ \frac{ik_X}{\epsilon_X} & \frac{-ik_X}{\epsilon_X} \end{bmatrix}, X_2 = \begin{bmatrix} e^{ik_X D_X} & e^{-ik_X D_X} \\ \frac{ik_X e^{ik_X D_X}}{\epsilon_X} & \frac{-ik_X e^{-ik_X D_X}}{\epsilon_X} \end{bmatrix} \tag{3.c}$$

$$M_1 = \begin{bmatrix} 1 & 1 \\ \frac{ik_M}{\epsilon_M} & \frac{-ik_M}{\epsilon_M} \end{bmatrix}, M_2 = \begin{bmatrix} e^{ik_M D_M} & e^{-ik_M D_M} \\ \frac{ik_M e^{ik_M D_M}}{\epsilon_M} & \frac{-ik_M e^{-ik_M D_M}}{\epsilon_M} \end{bmatrix} \tag{3.d}$$

For transverse electric (TE) polarized incident light, exactly the same results are obtained because planar designs show polarization insensitive characteristic under normal light incidence. Using these matrices and information of the dimensions and permittivity data of the materials, we can calculate the overall reflection from the structure, or we can numerically estimate the real and imaginary parts of ϵ_X to satisfy perfect absorption conditions (which is defined as $R < 0.1$).

2.2 Bruggeman's Effective Medium Theory

Effective medium approaches are developed to evaluate microscopically heterogeneous metal-dielectric composites as macroscopically uniform medium. These theories estimate the effective dielectric function of the composite in terms of the permittivities of the constituents in the composite and their filling fractions. The Maxwell-Garnett theory (MGT) and the Bruggeman's EMT are the most widely used approaches in this field [38]. MGT presents a solution for composites in which inclusions are embedded in the host material and have very low filling fraction. However, when constituents of the composite have a symmetric distribution and relatively comparable filling fractions, in other words, it is not obvious which material is the host, MGT fails and EMT has a successful approximation.

We start with applying Clausius-Mossotti relation [38] to a metal-dielectric composite. Permittivities and volume filling factors of the two constituents of the composite are ϵ_1 and ϵ_2, and f_1 and f_2, respectively. Host matrix has a permittivity of ϵ_h. In this case, Clausius-Mossotti relation is modified to

$$\frac{\epsilon - \epsilon_h}{\epsilon + 2\epsilon_h} = \frac{N_1\alpha_1}{3\epsilon_0\epsilon_h} + \frac{N_2\alpha_2}{3\epsilon_0\epsilon_h} \tag{4.a}$$

where N and α denotes volume density of the dipoles and polarizability of one molecule in a material, and ϵ is the effective permittivity of the composite, respectively. After some algebra, the equation (4.a) is arranged as

$$\frac{\epsilon - \epsilon_h}{\epsilon + 2\epsilon_h} = f_1\frac{\epsilon_1 - \epsilon_h}{\epsilon_1 + 2\epsilon_h} + f_2\frac{\epsilon_2 - \epsilon_h}{\epsilon_2 + 2\epsilon_h} \tag{4.b}$$

It should be noted that the two constituent materials are inclusions in the composite, which satisfy $f_1 + f_2 = 1$, and the host material is the composite itself; therefore, we set $\epsilon = \epsilon_h$. Equation (4.b) becomes that:

$$f_1\frac{\epsilon_1 - \epsilon}{\epsilon_1 + 2\epsilon} + f_2\frac{\epsilon_2 - \epsilon}{\epsilon_2 + 2\epsilon} = 0 \tag{5}$$

This is the final effective medium expression proposed by Bruggeman. It can be easily generalized to any number of constituents as follows:

$$\sum_i f_i\frac{\epsilon_i - \epsilon}{\epsilon_i + 2\epsilon} = 0, \sum_i f_i = 1 \tag{6}$$

The solution of equation (5) is

$$\epsilon = \frac{1}{4}((3f_1 - 1)\epsilon_1 + (3f_2 - 1)\epsilon_2 \pm \sqrt{((3f_1 - 1)\epsilon_1 + (3f_2 - 1)\epsilon_2)^2 + 8\epsilon_1\epsilon_2} \quad (7)$$

Causality requires positive imaginary part of the effective permittivity. The sign in the formula is chosen in order to make imaginary part positive to satisfy it.

Chapter 3

Simulation, Fabrication and Characterization Tools

In this chapter, we will discuss FDTD based commercial software of "Lumerical FDTD Solutions", fabrication and characterization equipment used in UNAM (National Nanotechnology Research Center) and NANOTAM (Nanotechnology Research Center) for research activities.

3.1 Simulation Software

FDTD is a numerical method to solve time-domain differential form of Maxwell's equations on a particular cell called Yee cell [39]. These equations are discretized using central-difference approximation both in time and space in a leap-frog scheme. Lumerical FDTD Solutions software presents a powerful 2-dimensional/3-dimensional(2D/3D) solver for nanophotonic devices. The simulation environment basically includes an FDTD region, a source, the design under consideration and power monitors, as shown in Figure 3.1. The drawn unit cell can be repeated infinitely many times using periodic boundary conditions on the sides. The bottom and top of the cell can be adjusted as perfectly matched layer

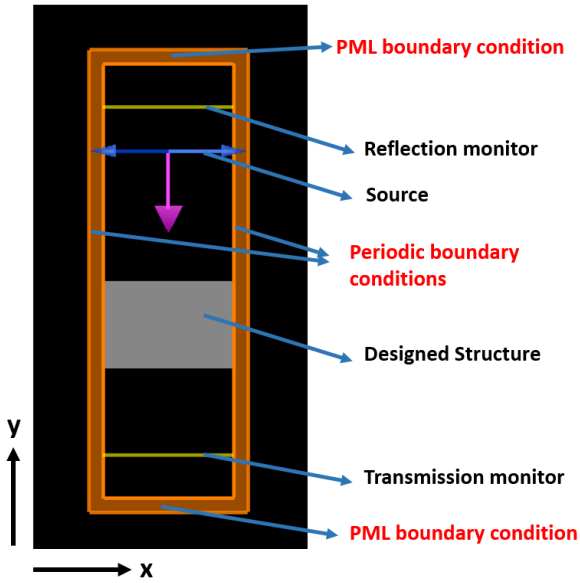

Figure 3.1: Lumerical FDTD Solutions simulation environment.

(PML) to mimic real environment. Figure 3.1 illustrates a simple 2D simulation environment with all the aforementioned components. An x-polarized (in other words, TM polarized) plane wave source is placed at the top to illuminate the sample with a broad wavelength spectrum. Two power monitors at the top and bottom are located to record reflection and transmission, respectively. The structure is drawn in the xy-plane (which is up to the user) since it is a 2D simulation. The boundaries in the x-direction are set as periodic to repeat unit cell infinitely many times, and the boundaries in the y-direction are set as PMLs. The software optimizes itself all FDTD parameters and converges successfully.

3.2 Fabrication Tools

In the fabrication route of the micro and nanophotonic devices, various deposition, etching and coating techniques and the corresponding equipment are utilized. In this section, the fundamental fabrication tools that I used in my research activities and basics of their operation mechanisms will be explained. These equipments

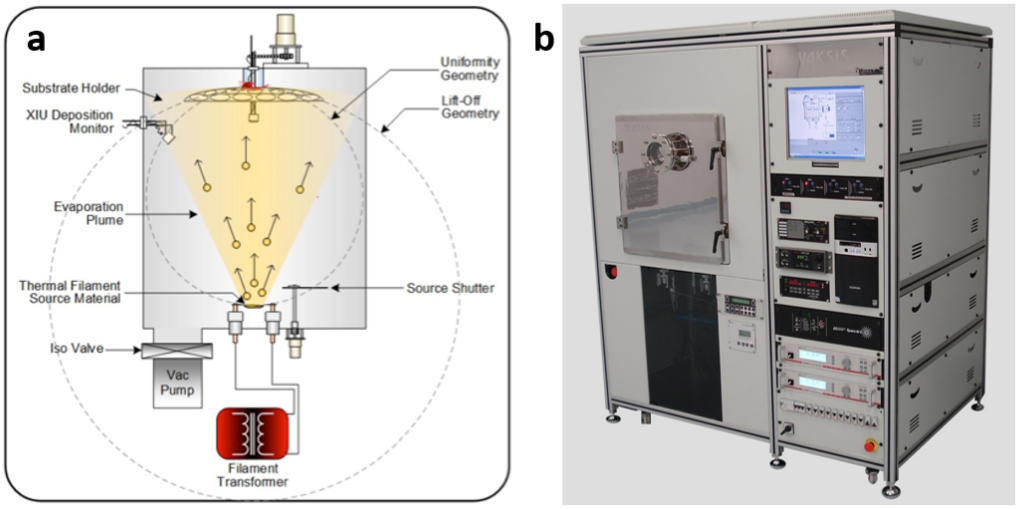

Figure 3.2: **(a)** Evaporation mechanism of thermal evaporator. **(b)** "MIDAS PVD 3T" model thermal evaporator of VAKSIS company.

are thermal evaporation, electron-beam evaporation and sputtering systems as physical vapor deposition (PVD) techniques and EBL.

3.2.1 Thermal Evaporation

Thermal evaporator is a simple PVD system that evaporates the material by extremely heating up to evaporation temperature with passing very high current through. The source material is put into a holder, which is heated by high voltages, at the bottom of the chamber. The sample is placed onto a rotating holder at the top. The chamber is vacuumed using a mechanical pump and turbo pump to achieve ultra-high vacuum conditions. When the vacuum level is satisfied (pressure is very low inside the chamber), mean free path of the molecules becomes in the order of few meters. This assures that evaporated molecules interact with each other at the minimum level, and so, coated on the sample. Power of the voltage source is increased to heat up the material holder and to start evaporation. The deposition rate and thickness are estimated by an acoustic sensor inside the chamber [40]. The complete scheme of the chamber and deposition mechanism is

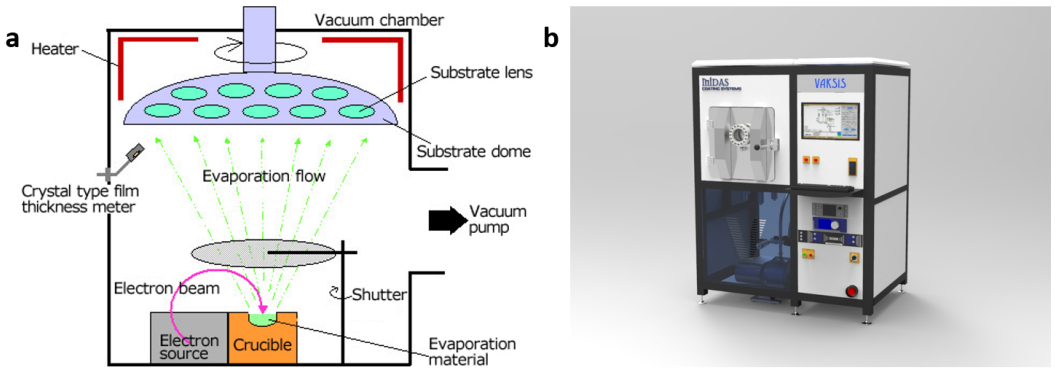

Figure 3.3: **(a)** Evaporation mechanism of electron beam evaporator. **(b)** "MIDAS PVD 1eB" model electron beam evaporator of VAKSIS company.

shown in Figure 3.2(a). We used "MIDAS PVD 3T" model of VAKSIS company, as shown in Figure 3.2(b).

3.2.2 Electron-beam Evaporation

Electron-beam evaporation technique works similar to thermal evaporation with the exception of using electron beams to evaporate the material. Evaporation process takes place under high vacuum conditions. High energy electron beams interact with the crucible material, lose their energy and heat up the source material. The crucible and electron gun are cooled by water circulation to prevent high temperatures. Evaporation rate and thickness are estimated by using a crystal sensor [40]. The general scheme of inside the chamber and an electron beam evaporator equipment of VAKSIS company are shown in Figure 3.3.

3.2.3 Sputtering

In sputtering technique, plasma of Argon gas is used to sputter target material and to deposit on the wafer. This technique is suitable to coat thin layers of various kinds of materials such as metals with high melting point and dielectrics.

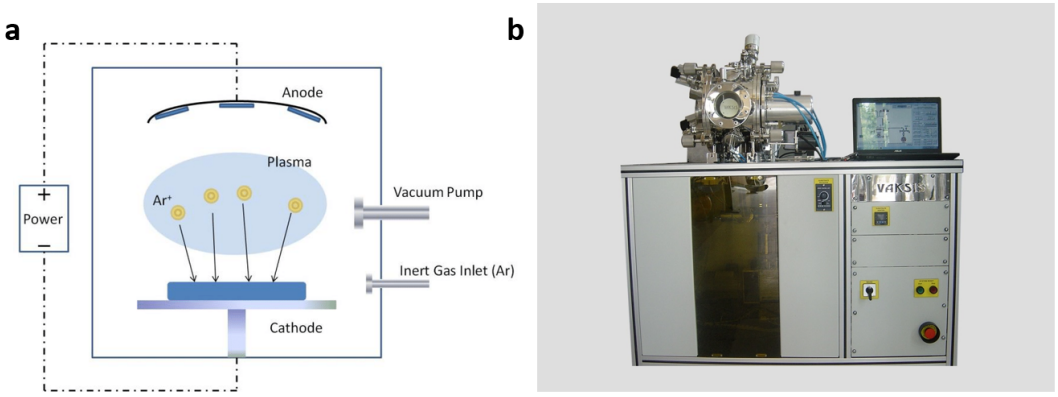

Figure 3.4: **(a)** Coating mechanism of sputtering systems. **(b)** "PVD Handy 3M" model sputtering of VAKSIS company.

It can be also utilized for deposition of alloys. RF Magnetron sputtering is the most widely used version for dielectrics [40]. Schematic of a DC sputtering system and a sputtering equipment of VAKSIS company are shown in Figure 3.4.

3.3 Characterization Tools

We used Fourier-Transform Infrared Spectroscopy (FTIR) for normal incidence characterization and Ellipsometer for oblique incidence characterization to find reflection and transmission measurements of the sample. Also, Environmental Scanning Electron Microscopy (E-SEM) was used to image and evaluate perfection of fabricated structures.

3.3.1 Fourier-Transform Infrared Spectroscopy

FTIR can measure reflection, transmission or emission of a sample in Vis, NIR and MIR regimes. Characterization of the sample is carried out for a broad wavelength range at one measurement. Therefore, it measures the samples in a brief time and in a very accurate way. The working principle of the equipment depends on

Figure 3.5: Bruker - Vertex 70v and Hyperion microscope

Michelson interferometer. The infrared energy is emitted from a glowing blackbody source. Three different beam splitters are used for each regime: Quartz for Vis, calcium fluoride (CaF_2) for NIR, and potassium bromide (KBr) for MIR. Four different detectors are used to measure reflection and transmission data from the sample: silicon diode for Vis, indium gallium arsenide (InGaAs) for NIR, and mercury cadmium telluride (MCT) D313 and D316 for MIR [41]. We used "Bruker-Vertex 70v, Hyperion microscope" model, as shown in Fig. 3.5.

3.3.2 Ellipsometer

Ellipsometer is an efficient tool to measure the overall reflection from the sample at oblique incidence, to measure transmission through the sample, to find deposition thickness of a layer, or to extract refractive indices of any type of a material with modeling. The general operation mechanism of the ellipsometer is shown in Figure 3.6(a). The incident light generated from the source goes through a polarization generator. Reflection from the surface changes polarization of the light in terms of amplitude and phase. The changes in the polarization are analyzed and detected in the detector [41].

There are two primary working options of the equipment. "R&T Scan" mode

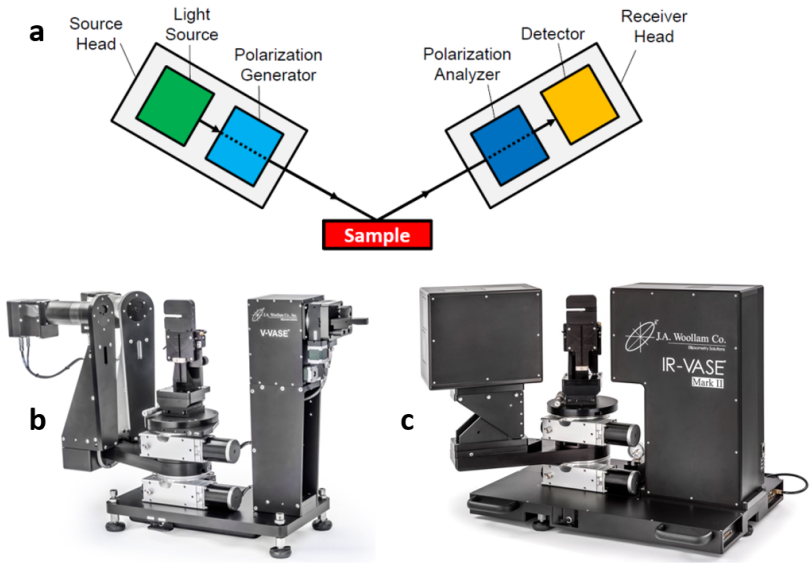

Figure 3.6: **(a)** General scheme of an ellisometer. **(b)** V-VASE and **(b)** IR-VASE model of J.A. Woollam Co. Inc.

illuminates the sample in different angles with TE and TM polarized light to find the normalized reflection and transmission of the sample. "Spectroscopic Scan" mode of the device measures the change in polarization of the incident light as a result of interaction with the sample. The equipment records two parameter of the detected light: amplitude ratio (ψ) and phase shift (Δ). After modeling of the saved data is carried out with a sufficiently low mean squared error (MSE), the thicknesses of each layer and refractive indices are obtained. There are many oscillator functions such as Drude, Lorentz, Gaussian and Cauchy oscillator available in the library. We used J.A. Woollam Co. Inc. V-VASE and IR-VASE ellipsometers, as shown in Figure 3.6(b-c).

3.3.3 Environmental Scanning Electron Microscopy

SEM is an electron microscope that produces image and identifies composition of the sample surface by scanning with focused electron beams. Electrons have much shorter wavelengths than white light, which enables resolution better than 1 nm. The main components of SEM are electron source, lens system to focus

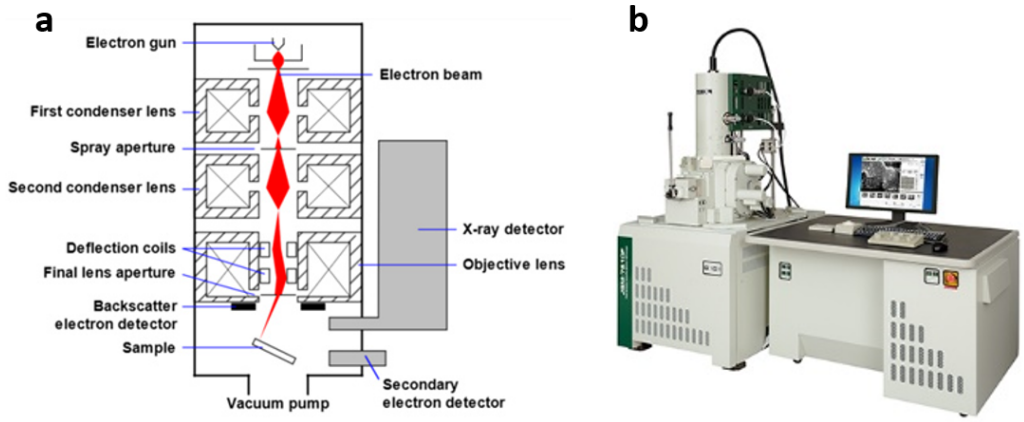

Figure 3.7: **(a)** General scheme of the SEM chamber. **(b)** JSM-7610F Schottky Field Emission Scanning Electron Microscope.

electron beam onto the surface, sample chamber, electron detector and a computer and visualization tool. Electrons generated at the top of the source column, are accelerated under high voltages ($\sim$10 kV), and pass through a condenser lens and aperture system to be focused on the sample surface. As a result of interaction between focused electron beam and the sample mounted on a stage, secondary electrons, backscattered electrons and characteristic X-rays are scattered from the surface. These particles are collected by detectors and image of the surface is produced after analysis in a computer. Electron beams can penetrate to a few microns deep of the surface, which allows to analyze material composition of the sample [41]. A rough schematic of an SEM and an example of the equipment are shown in Figure 3.7(a-b).

Chapter 4

All-Ceramic Based Metal-free Ultra-broadband Perfect Absorber

This chapter bases on the publication "All-Ceramic Based Metal-free Ultra-broadband Perfect Absorber" by M.C. Soydan et al. in Plasmonics (2019). Reproduced (or Reproduced in part) with permission from Springer Nature and Copyright Clearance Center.

4.1 Preface to Broadband Perfect Absorber Designs

A high-performance light absorber is one of the most studied topics in nanophotonics, leading to different attempts to devise perfect light absorbers, operating either in narrowband or broadband frequency regimes, by using various materials and structures. As explained in Chapter 1, perfect absorbers have a variety

of applications in research areas such as sensing [42], spectroscopy [43], photovoltaic [22] and thermal photovoltaic [24], solar vapor generation as well as photodetection [44]. Metamaterials, with their exceptional properties that cannot be observed in nature, are of great use for the purpose of designing the optimum perfect absorber. One of the most commonly used structure in order to achieve near unity light absorption is metal-dielectric-metal (MDM) architecture [45, 46, 47, 48, 49, 50, 51, 52, 53, 54, 55, 56]. In this structure, dielectric films are sandwiched by a patterned metal film and a flat thick metal layer. The insertion of the dielectric layer between thin metal layers boosts the absorption of the structure by efficiently coupling of incident light into the cavity modes of the MDM design. The bottom metal layer acts as an ideal mirror that reflects all incoming wave back into the cavity, and the top metallic patterned layer includes nanoresonant units to couple the light inside the structure. To improve the bandwidth (BW) of a perfect absorber, different patterning structures such as nanopatches [57, 58, 59], nanodiscs [46, 60] or nanorings [61] were developed. These structures can behave as ultra-broadband [51, 52, 53, 54, 55] as well as narrowband [50] perfect absorbers, and can carry properties such as polarization-independence [54, 55, 56] and angle-tolerance [62] depending on the pattern of the top layer and thickness of the dielectric layer. Although great performances can be attained with these structures, they are large scale incompatible because EBL is required to fabricate the patterned top layer.

In a recent study, it was theoretically and experimentally demonstrated that the use of planar metal-dielectric (MD) pair multilayer design can provide an ultra-broadband light absorption [63]. Many planar, lithography-free and high performance designs were developed and fabricated using this configuration [64, 65, 66, 37] because it has an obvious advantage of ease of fabrication, and thus, large scale compatibility. Later, some studies revealed that the light absorption spectrum can be extended using hyperbolic metamaterials (HMMs) [67, 68, 69, 70, 71, 72]. A substantial improvement in the absorption BW could be acquired by tapering this multilayer design. The tapered shape enables coupling of the incident photons in a wide frequency range by gradual matching of the air impedance into the underlying metamaterial configuration [73]. Lei et al.

realized an angle-tolerant, polarization-insensitive and omnidirectional absorber from 200 nm to 3.6 μm using an HMM structure with alternating 20 pairs of aluminium (Al) and germanium (Ge) multilayered films [67]. Besides all these improvements in perfect absorbers, these multilayer designs suffer from multiple depositions and complex processes that limit their applicability for large scale applications. Moreover, in many applications such as thermal photovoltaic and solar vapour generation, the high operation temperature could deform the layers. A better option for designing such ultra-broadband absorbers is to replace metals with a high temperature tolerant medium since metals have an inherent lossy nature and exposed to erosion and oxidation under temperature and humidity.

Ceramic materials are the suitable choices to be used instead of metals to improve the performance of the designed structure because ceramics have less lossy nature, a higher melting point compared to noble metals, and more durability against oxidation and corrosion. In recent years, titanium nitride (TiN) has become a promising alternative to metals and has been successfully integrated in metal-free metamaterial designs in some studies [74, 75, 76, 77, 78, 79, 80]. Recent reviews also highlighted the tremendous potential of these ceramics in different light-matter interaction applications [81, 82, 83, 84, 85]. Taking all of these into account, it is of great importance to design a ceramic based ultrathin design configuration to realize perfect light absorption in an ultra-broadband wavelength regime where both optical and thermal properties of the metamaterial design will be simultaneously satisfied.

4.2 Motivation and Novelty

In this work, we reveal the high potential of transition metal carbides (TMCs) and nitrides (TMNs) to be used instead of metals in ultra-broadband perfect absorbers making use of their excellent thermal properties (e.g., extremely high melting point) and superior absorption performance compared to metals in any configuration. For this purpose, we propose ultra-broadband near unity light absorber designs based on TMC (or TMN) in two different configurations; planar

and trapezoidal MD pairs based array structure, and compare the performance of the proposed designs with metallic based corresponding. We use titanium carbide (TiC) and vanadium carbide (VC) as TMC, TiN and vanadium nitride (VN) as TMN, and aluminum oxide (Al_2O_3), silicon dioxide (SiO_2) and titanium dioxide (TiO_2) as the insulator material. Also different lossy metals such as titanium (Ti), platinum (Pt) and nickel (Ni) are used to compare the performance of metallic-based and ceramic-based designs. This chapter is organized as follows: In the first part of this chapter, a systematic modeling approach based on TMM is carried out to reveal compatibility of permittivity data of TMCs and TMNs for broadband perfect absorber designs. Afterwards, by conducting FDTD method is employed to find the optimal geometries for each TiC/VC/TiN/VN and Al_2O_3 pairs in planar metal-dielectric-metal-dielectric (MDMD) configuration separately to obtain the broadest attainable absorption spectrum. It is shown that TiC-Al_2O_3 pair offers the best performance among these materials with an absorption BW as wide as 1090 nm covering from 405 nm to 1495 nm with an average absorption value of 0.95. This BW is not only significantly wider than TiN based multilayer designs [74, 78], but also larger than that of the highest reported BW for a metal based MDMD configuration, where a wavelength range of 400 nm-1400 nm was absorbed utilizing the optimal case of a chromium(Cr)-SiO_2 multilayer configuration [86]. Next, trapezoidal array structure is proposed as an option to increase the absorption BW of the design. Geometries of the structure were optimized in a similar fashion for each pair of TMCs/TMNs/metals and Al_2O_3 separately when 3 MD-pair trapezoidal array structure is in use. VN-Al_2O_3 pair offered the strongest absorption profile with an amount above 0.9 in the wavelength range from 300 nm to 2500 nm, with a BW of 2200 nm, which is much wider than the BW of metallic designs. In addition, possible fabrication inaccuracies are considered, their possible effects are scrutinized and an alternative design is proposed to preserve the same performance for trapezoidal array structure. Considering their optical and thermal properties, TMCs and TMNs are excellent choices for thermophotovoltaic and solar vapor generation applications where both high optical absorption and long-term durability can be acquired.

4.3 Theoretical Analysis

The schematic illustration of the first proposed multilayer structure is depicted in Figure 4.1(a). According to this panel, the structure mainly consists of two MD pairs, which are comprised of the same materials, stacked on top of each other. The bottom metal layer is thick enough to act as a perfect mirror that reflects all the light back into the cavity. The bottom insulator layer acts as a spacer between the bottom and middle metal layers in order to create an MDM cavity. The top insulator layer, added onto the MDM cavity, behaves like a broadband antireflective coating to match air impedance to that of an underneath metal layer.

In this design, the operational performance of the multilayer is mainly determined by the middle metal layer. The thickness and type of this metal have to be selected in such a way that it should be thin enough to allow light penetration into the cavity and it should be thick enough to trap the light inside of it. For the starting point in designing the multilayer perfect absorber, we first adopted a modeling approach to find the ideal material for the middle layer in which the overall reflection from the MDMD structure is zero. To achieve this goal, the TMM was carried out to find the overall reflection from the design. The generalized case of TMM, described in chapter 2, was adapted to a 4-layer MDMD design. For the TM polarization, H_{y} in that structure becomes that

$$H_y(z) = \left\{ \begin{array}{cc} A_i e^{ik_A z} + A_r e^{-ik_A z}, & z < 0 \\ D_{11} e^{ik_D z} + D_{12} e^{-ik_D z}, & 0 < z < D_D \\ M_{11} e^{ik_M (z-D_D)} + M_{11} e^{-ik_M (z-D_D)}, & D_D < z < D_D + D_M \\ D_{21} e^{ik_D [z-(D_D+D_M)]} + D_{22} e^{-ik_D [z-(D_D+D_M)]}, & D_D + D_M < z < 2D_D + D_M \\ M_{21} e^{ik_M [z-(2D_D+D_R)]} + M_{22} e^{-ik_M [z-(2D_D+D_R)]}, & 2D_D + D_M < z < 2D_D + D_M + D_R \\ A_t e^{ik_A [z-(2D_D+D_R)]}, & z > 2D_D + D_M + D_R \end{array} \right\} \quad (1)$$

and applying the appropriate boundary conditions, reflection of the incident

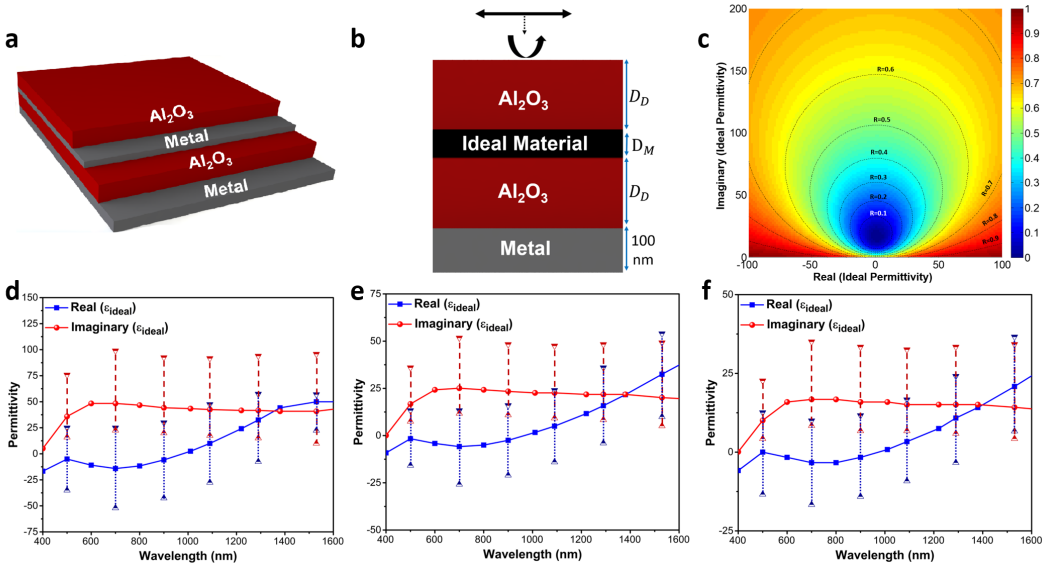

Figure 4.1: **Designed structure and ideal material.** Schematic illustration of the proposed **(a)** multilayer structure and **(b)** setup to obtain ideal middle layer. Part **(c)** depicts the contour plot for reflection value as a function of real and imaginary parts of permittivity for a 10 nm ideal middle layer at the wavelength of 1000 nm. Zero reflection point (ZRP) values and tolerable region for $R < 0.1$ for different middle layer thickness of **(d)** 5 nm, **(e)** 10 nm, and **(f)** 15 nm are also displayed.

light from the structure can be obtained as $R = |\frac{F_{11}}{F_{12}}|^2$. Here, $F = \begin{bmatrix} F_{11} \\ F_{12} \end{bmatrix} = a_1^{-1} d_1 d_2^{-1} m_1 m_2^{-1} d_1 d_2^{-1} a_2$ where:

$$a_1 = \begin{bmatrix} 1 & 1 \\ \frac{ik_A}{\epsilon_A} & \frac{-ik_A}{\epsilon_A} \end{bmatrix}, a_2 = \begin{bmatrix} 1 \\ \frac{ik_A}{\epsilon_A} \end{bmatrix} \tag{2.a}$$

$$d_1 = \begin{bmatrix} 1 & 1 \\ \frac{ik_D}{\epsilon_D} & \frac{-ik_D}{\epsilon_D} \end{bmatrix}, d_2 = \begin{bmatrix} e^{ik_D D_D} & e^{-ik_D D_D} \\ \frac{ik_D e^{ik_D D_D}}{\epsilon_D} & \frac{-ik_D e^{-ik_D D_D}}{\epsilon_D} \end{bmatrix} \tag{2.b}$$

$$m_1 = \begin{bmatrix} 1 & 1 \\ \frac{ik_M}{\epsilon_M} & \frac{-ik_M}{\epsilon_M} \end{bmatrix}, m_2 = \begin{bmatrix} e^{ik_M D_M} & e^{-ik_M D_M} \\ \frac{ik_M e^{ik_M D_M}}{\epsilon_M} & \frac{-ik_M e^{-ik_M D_M}}{\epsilon_M} \end{bmatrix} \tag{2.c}$$

and $k_{i=(A,D,M)} = \sqrt{\frac{\epsilon_i \omega^2}{c^2} - k_x^2}$ where c is the speed of light, A, D and M represents air, dielectric and metal, respectively. Moreover, D_D, D_M and D_R are the thicknesses of the dielectric, middle material and reflector layers, and ϵ_{D} and ϵ_{M} are permittivities of the dielectric and metal, respectively. As illustrated in Figure 4.1(b), the proposed structure has Pt (with a thickness of 100 nm) as the back reflector material (i.e., thick bottom metal layer). It should be mentioned that in this section our aim is to find the best middle layer and bottom layer is only a reflecting coating. Therefore, in all cases, in this part, the Pt layer is kept as bottom layer. Two identical Al_2O_3 layers with the same thickness of 80 nm have sandwiched the middle ideal metal layer. For each wavelength, the real and imaginary parts of permittivity of the ideal middle material are found in a way that the overall reflection from the stack is zero. Figure 4.1(c) illustrates the contour plot of the reflection (R) as a function of the real and imaginary parts of permittivity for a 10 nm thick middle layer at the $\lambda = 1000nm$. This plot clearly shows a group of centric circles around the zero reflection point (ZRP) where these circles radii get enlarged for larger values of R. Therefore, to be able to retain reflection below $R = 0.1$, the permittivity values (real and imaginary parts) for the middle layer should be located inside the $R = 0.1$ circle. To gain a better insight, the values for ZRPs of an ideal metal with thicknesses of $D_M = 5nm, 10nm, 15nm$ are plotted at Figures 4.1(d-f), respectively. The error bars are also utilized in these panels to define the range of values for the real and imaginary parts of permittivity where the reflection stays below 0.1 (more than 90 percent absorption). As these results illustrate, to have an ideal metal, the real part of the middle layer permittivity should take small values around zero (positive or negative) for $\lambda < 1000nm$ and this trend gradually grows toward positive values for longer wavelengths. This is actually the main reason that restricts the absorption capacity of metal based multilayer designs since, for most of the metals, the real part of permittivity exponentially approaches large negative values as we move toward longer wavelengths. However, the imaginary part shows a relatively flatter response over the entire wavelength range except the shorter wavelengths ($\lambda < 600nm$) where the values start to gradually grow from around zero to the flat response point. Moreover, comparing the extracted values for different metal thickness shows that the ZRPs are larger for thinner

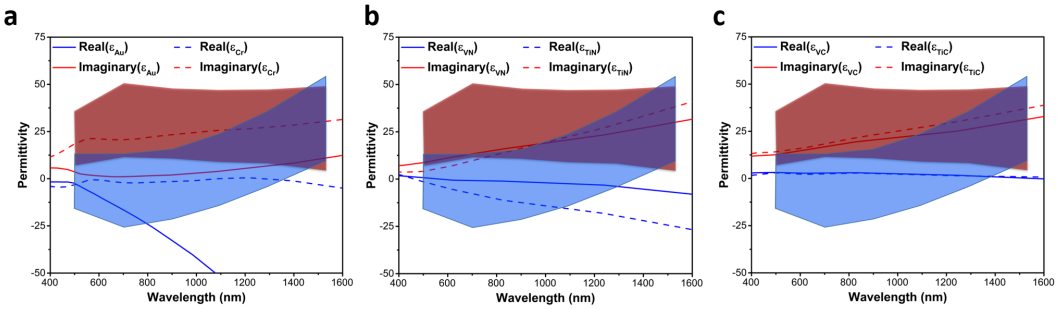

Figure 4.2: **Ideal permittivity region for perfect absorption.** Comparison between real and imaginary parts of permittivity between **(a)** Au and Cr, **(b)** VN and TiN, and **(c)** VC and TiC and ideal case. The blue and red highlighted regions are tolerable real and imaginary values for $R < 0.1$, respectively.

metal layers but at the same time the range of acceptable values for $R < 0.1$ is much wider. The situation is vice versa for thicker ideal metal layers. Therefore, to guarantee a reflection below 0.1, we need to choose our material in a way that its permittivity values are within the proposed range.

Some nonstoichiometric ceramic materials including transition-metal carbides and nitrides show high carrier concentration and demonstrate an optical performance that is close to metals. However, in general, the real part of their permittivities for these dielectric materials are more close to zero (at the negative side). Therefore, it is expected that these materials can be an excellent option to replace metal based multilayer absorbers. The comparison, on how well different metals, carbides, and nitrides are matched to this ideal model, is presented in Figures 4.2(a-c). The blue and red highlighted areas are the set of tolerable values for the real and imaginary parts of the permittivity of a 10 nm thick ideal material that provide a reflection below $R < 0.1$. In this work, among other transition metal nitrides, VN and TiN are chosen to be explored. In the case of carbides, VC and TiC have been the choices of study. Figure 4.2(a) compares the permittivity values for Cr and Au with the ideal case. The permittivity values of Au and Cr have been obtained from CRC model. As it can be clearly seen, Au shows very poor agreement for both real and imaginary parts while permittivity values of Cr fairly meets the tolerable region for $\lambda < 1350nm$. In fact, this mismatch is raised from the real part of the permittivity not that of its imaginary part.

These findings from modeling are in agreement with what was obtained from the experimental results [86]. The results for the case of carbides and nitrides have been also depicted in Figures 4.2(b-c). The permittivity values for these four different materials have been taken from the works of Pflüger et al. [87, 88]. In the case of nitride based materials, the real part of permittivity for VN crosses the border of the highlighted region in longer wavelengths compared to that of TiN. Furthermore, while the imaginary part is entirely inside the filled area for VN, it slightly stays out of the region for $\lambda < 750nm$ in the case of TiN. This matching is the best for the case of transition metal carbide materials. Figure 4.2(c) points out the real and imaginary parts of permittivities of VC and TiC retained within the range up to 1380 nm. These results clearly elucidate the fact that transition metal carbides and nitrides are excellent choices to replace metals for perfect absorber applications. In addition to their unprecedented optical behavior, these ceramic materials have superior thermal and chemical stability and they are refractory materials with an extremely high melting point that is a main factor to define the long-term stability of an absorber device. For example, Cr has a melting point of 1907^oC while this value for TiC is 3160^oC.

4.4 Designed Structure and Simulation Setup

To evaluate our modeling results, we conducted numerical simulations to find the optimal configuration for each of the above materials. The role of different thicknesses in the overall absorption capability of the stack was scrutinized in the first step by employing numerical calculations using the commercial FDTD software package (Lumerical FDTD Solutions). Throughout the simulations, the propagation direction of incident light was fixed to be perpendicular to the xy plane. A broad plane wave with a linear x-polarized E field was being utilized to excite the unit cell and reflected (R) and transmitted (T) lights were recorded by two frequency domain power monitors on two sides of the multilayer structure. Periodic boundary conditions were also employed in the $x-$ and $y-$ directions, while boundaries in the z direction were adopted as a PML. 1 nm sized mesh was added to the related simulation region in both the $x-$ and $y-$directions.

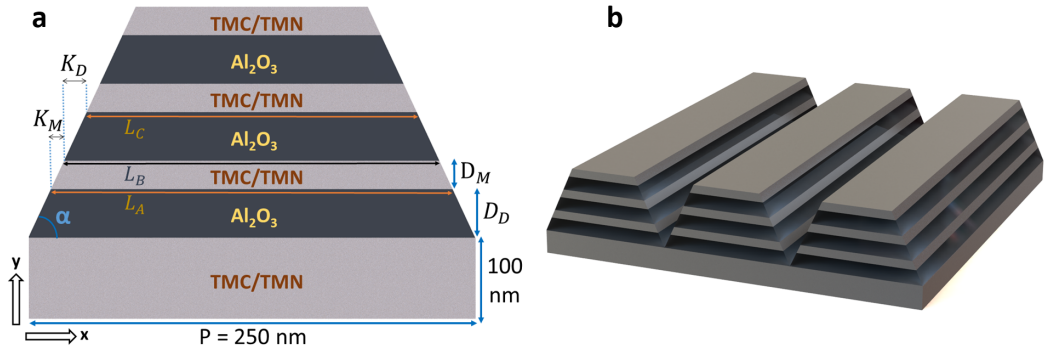

Figure 4.3: **Schematic illustration of the proposed trapezoidal MD pair array design (a)**Unit cell of the structure in 2D. **(b)** Perspective view of the structure in 3D.

The refractive index data of the TMCs and TMNs is fitted using the "Material Explorer" tool of the FDTD Solutions. Using fit tolerance as 0.0001 and max coefficients as 20, the materials were modeled closer to the material data in a better function. The simulations were performed with this fitted model.

The 2D view of the planar MDMD array and 2D and 3D views of the designed trapezoidal MD pairs array structure are illustrated in Figure 4.1(b) and Figure 4.3, respectively. They consist of alternating TMC (or TMN) and dielectric layers and TMC (or TMN) substrate. While planar configuration has two parameters, which are D_D and D_M, to be optimized, trapezoidal array configuration has four parameters, which are D_D, D_M, side wall angle of the trapezoid design (α), and periodicity (P). Periodicity was kept at 250 nm and the geometries of the design were optimized by altering other parameters for each TMC, TMN, and metal. The main goal of this design is to cover the visible region and possible longest wavelength with near unity absorption.

The trapezoidal structure does not have a fine tip, but a tapered top layer. The width of the top layer is set by the side-wall angles, where the bottom width of the trapezoid is the same as the P. The side wall angle can be calculated from the equation of $\alpha = \arctan\frac{D_\mathrm{M}}{K_\mathrm{M}} = \arctan\frac{D_D}{K_\mathrm{D}}$ where K_M and K_D are the half of difference between bottom lengths of subsequent metallic and dielectric layers (L_A is bottom length of dielectric layer, L_B is bottom length of upper metal layer,

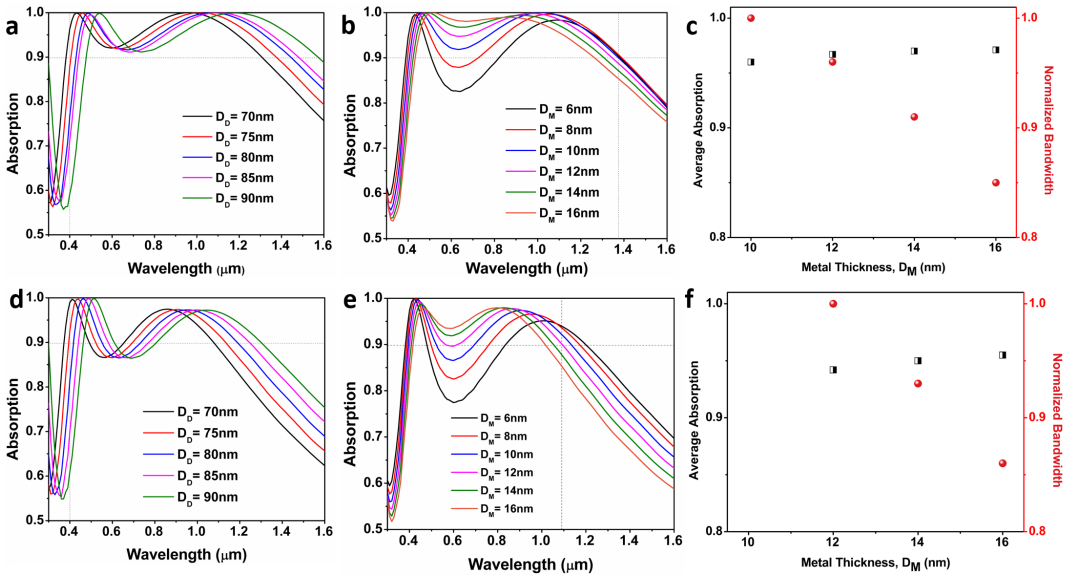

Figure 4.4: **Parameter optimization of nitride materials** The impact of **(a)** dielectric thickness and **(b)** middle layer thickness in the absorption capability of the multilayer and **(c)** average light absorption and normalized BW for different material thickness in the case of VN multilayer. The impact of **(d)** dielectric thickness and **(e)** middle layer thickness in absorption response of the multilayer and **(f)** average absorption and normalized BW values for different TiN thickness.

and L_{C} is bottom length of upper dielectric layer), as shown in Figure 4.3(a). To be clear, if we call bottom and top width of a TMC/TMN layer as L_{A} and L_{B}, respectively, and top width of the upper dielectric layer as L_{C}, mathematically, $K_M = \frac{L_A - L_B}{2}, K_D = \frac{L_B - L_C}{2}$. K_{M} and K_{D} values are different to keep the side-wall angle constant since the thickness of the layers are different.

Absorption (A) was calculated using the equation of $A = 1 - R - T$. Considering the fact that the bottom reflecting layer thickness is much thicker than that of light skin depth at our operation frequencies, we can suppose T to be zero (this has been verified during our simulations). Consequently, the absorption can be found by the following simplified equation of $A \cong 1 - R$.

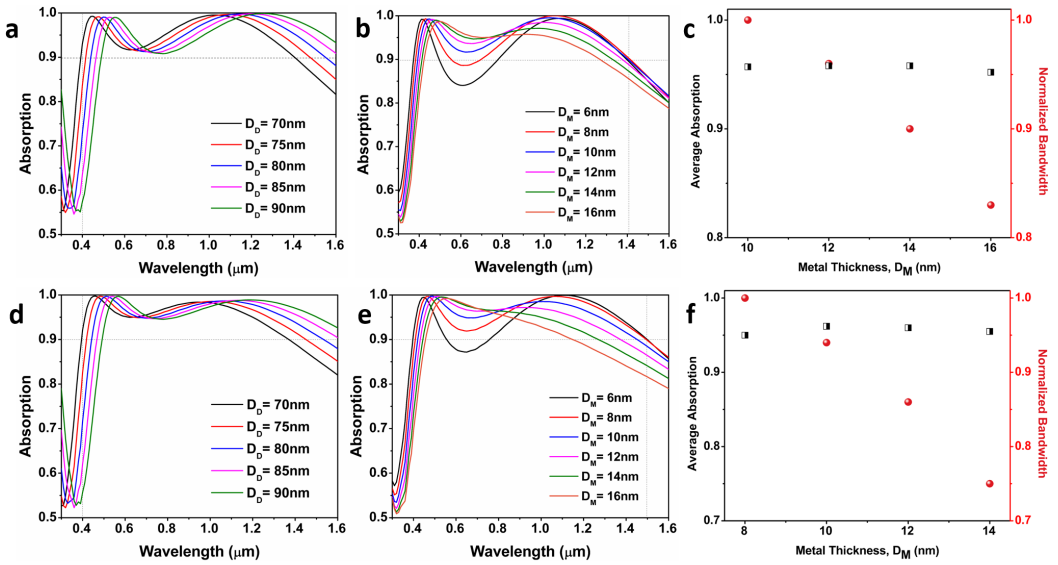

Figure 4.5: **Parameter optimization of nitride materials** The impact of **(a)** dielectric thickness and **(b)** middle layer thickness in absorption capability of the multilayer and **(c)** average light absorption and normalized BW for different material thickness in the case of VC multilayer. The impact of **(d)** dielectric thickness and **(e)** middle layer thickness in absorption response of the multilayer and **(f)** average absorption and normalized BW values for different TiC thickness.

4.5 Simulation Results & Discussion

4.5.1 In Planar MDMD Architecture

In planar MDMD configuration, we first optimized D_D in a way that the perfect absorption covers the whole visible range for all of the cases. In other words, its lower edge should be located at around 400 nm. During this optimization step, D_M was fixed at 10 nm. Taking $A = 0.9$ as the BW threshold, we can also define the upper edge of the regime. It should be noted that in all of the simulations the configuration has four layers. The bottom layer was chosen to be the same as the middle material coating with a thickness of 100 nm. Throughout this section, $D_D - D_M - D_D$ annotation was employed to refer to a configuration of planar array (as an example, 75-10-75 means the dielectric layer thicknesses are 75 nm and the middle layer is 10 nm thick). Figures 4.4(a-c) show the results for

VN absorbing layer. According to the Figure 4.4(a), to ensure complete visible regime coverage, the thickness of the Al_2O_3 was fixed at 75 nm and to optimize the absorption BW and strength, thickness of the metal was swept from 6 nm to 16 nm, as shown in Figure 4.4(b). According to these panels, the largest BW belongs to 75-10-75 configuration covering from 405 nm to 1375 nm with an overall BW of 970 nm. To have a better qualitative comparison, the normalized BW values for different metal thicknesses are presented in Figure 4.4(c). The BW of the multilayer is decreased to 0.85 moving from the metal thickness of 10 nm to 16 nm. In addition to this, the average absorption over the corresponding BW of each configuration is calculated and plotted in this figure. As it can be clearly seen, the average absorptions for all the cases are above 0.96 which proves a near unity absorption from this configuration. The corresponding results for TiN case is also presented in Figures 4.4(d-f). Choosing the Al_2O_3 dielectric layer thickness (D_D) as 75 nm, the best performance was attained in the material thickness of $D_D = 12nm$ in which a BW of 695 nm can be accomplished (400 nm-1095 nm). Using this number as a normalization factor, the BW drop trend for thicker layers was also depicted in Fig 4(f). For this material, the average absorption stays above 0.94 throughout its operation BW. These results are also in line with our findings discussed in the modeling section. For instance, based on our theoretical calculations, the imaginary part of permittivity of TiN stays out of the $R < 0.1$ region for $500nm < \lambda < 800nm$. This can be confirmed by our numerical simulations where a dip in the absorption spectrum was observed in this wavelength range. Moreover, the fact that the absorption upper edge was located at longer wavelengths in the case of VN is also predicted by Figure 4.2(b). It is noteworthy that the theoretical findings have assumed an Al_2O_3 dielectric thickness of 80 nm while the results at Figure 4.4 are found for optimal D_D thickness of 75 nm. The same systematic study was also carried out for carbide materials. The optical behaviour for carbides is even better as shown in Figures 4.5(a-f). For the case of VC, in the optimal configuration of 75-10-75, the multilayer stack absorbs light over a broad wavelength regime of 415 nm-1480 nm that corresponds to a BW of 1065 nm. Similar to VC, TiC has also superior light absorption capability, introducing absorption above 0.9 from 405 nm up to 1495 nm. In fact, the optimal multilayer configuration of 75-8-75 for TiC has the

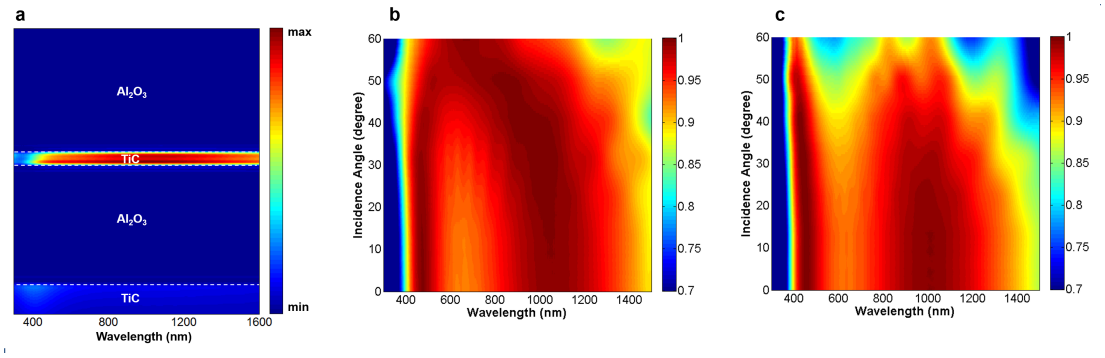

Figure 4.6: **Absorbed power and polarization dependency.** **(a)** The contour plot comparing the absorbed power in different parts of MIMI design. The absorption values for **(b)** TM and **(c)** TE polarization for oblique incidence angles of $0^o < \theta < 60^o$.

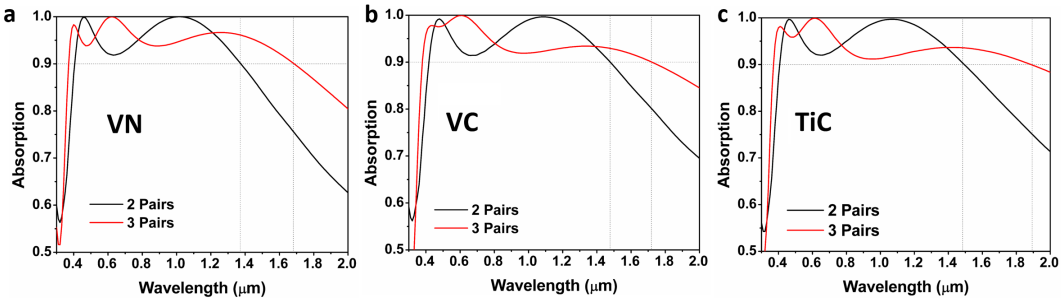

Figure 4.7: **BW improvement with increasing number of pairs.** The absorption spectra of 2 pairs (MDMD) and 3 pairs (MDMDMD) configurations for the cases of **(a)** VN, **(b)** VC, and **(c)** TiC multilayers.

highest BW among all of the other choices with an average absorption above 0.95 throughout its BW, which is also wider than reported highest BW of metal based MDMD designs, where a range from 400 nm to 1400 nm is absorbed utilizing the Cr-SiO_2 multilayer configuration [86].

To elucidate the mechanism of the absorption in this multilayer geometry, a contour plot displaying the amount of absorbed light in different parts of a multilayer for the optimal case of TiC is plotted in Figure 4.6(a). As it can be clearly deduced from this panel, most of the light is concentrated in the middle absorbing layer. This is an expected result taking the high absorption coefficient of the nitride and carbide materials. Moreover, only a small portion of light in the

lower wavelength values is absorbed using the bottom reflector layer. The oblique angle absorption response of the multilayer design is also plotted in Figures 4.6(b-c) for TM and TE polarization cases. As it is clearly illustrated in this figure, when the light is incident at wider angles, both the upper and lower edges of the absorption approach each other and, consequently, the absorption BW gets smaller. This case is more pronounced in the case of TE polarized incident light. However, in general, the absorber keeps its light absorption capability high over all oblique angles. This shows that this structure is not only an ultra-broadband absorber but also it shows a wide angle response over all incident angles.

Light absorption BW can be further extended utilizing larger number of MD pairs. Figures 4.7(a-c) depict the absorption spectra for MDMD and MDMDMD configurations for three optimal cases of VN, VC, and TiC. For both configurations, the thicknesses of layers are chosen as their optimal values found in the previous part. As Figure 4.7(a) shows, the absorption BW can be extended to 1685 nm using 3-pair multilayer architecture. An upper wavelength edge, as long as 1715 nm, can be obtained by employing VC based MDMDMD configuration, see Figure 4.7(b). BW extension is the largest for TiC where the absorption above 0.9 can be achieved in a wavelength range of 370 nm–1895 nm (Figure 4.7(c)). These findings reveal the capability of these materials to absorb light in an ultra-broadband regime where adding the number of pairs can extend the absorption BW toward longer wavelengths. However, a better approach to achieve broadest absorption response, while keeping the overall thickness the same, is to use tapered multilayer designs instead of planar ones. Therefore, a trapezoidal array structure comprised of 3 MD-pairs was designed and optimized for each TMC and TMN material to present higher performance of metal-free ultra-broadband perfect absorbers, and to reveal their superiority over commonly used metals.

4.5.2 In Trapezoidal Array Architecture

In the MD pairs based trapezoidal array structure, we initially attained a good absorber using cursory parameters to understand the capability of the material

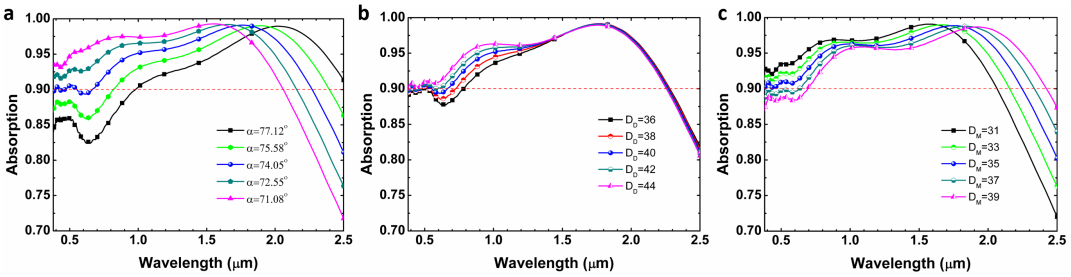

Figure 4.8: **Optimization process of TiC. (a)** The impact of α when other parameters are $D_{\mathrm{M}} = 35nm, D_{\mathrm{D}} = 40nm$. **(b)** The impact of the thickness of the dielectric layer when other parameters are $D_{\mathrm{M}} = 35nm, \alpha = 74.05^o$. **(c)** The impact of the thickness of TiC layer when other parameters are $D_{\mathrm{D}} = 44nm, \alpha = 74.05^o$.

in that geometrical shape. After the first set of results were obtained for each material, they were optimized in order to obtain the broadest absorption band. In all of the cases, we first optimized the side wall angle of the trapezoid since a change in the optimal angle influences optimum values of the other parameters. Then, D_D was optimized considering that perfect absorption (above 0.9) is achieved in the visible region because D_D has a determining effect on the absorption at shorter wavelengths. Afterwards, D_M was optimized to have the broadest band. All of the structures were designed at the same period which is 250 nm. The designed structure for different materials was optimized in a way that its absorption spectrum fully covers the visible region and reaches to the possible longest wavelength. It should be noted that all of the simulations were carried out under TM polarized incident light. For TE polarization, absorption spectra becomes different.

Figures 4.8(a-c) demonstrate the optimization process of the TiC. The first result is obtained when $D_{\mathrm{M}} = 35nm, D_{\mathrm{D}} = 40nm, \alpha = 74.05^o$ and then α, D_D and D_M were optimized, respectively. According to Figure 4.8(a), side wall angle of the trapezoid can be chosen either 74.05^o or 72.55^o since their results are above the 0.9 absorption. For $\alpha = 74.05^o$, absorption decreases to below 0.9 at some wavelengths; however, it can be compensated with altering the thicknesses of the dielectric and TiC layers. Considering the purpose of having the largest BW, the $\alpha = 74.05^o$ side wall angle has better performance compared to the

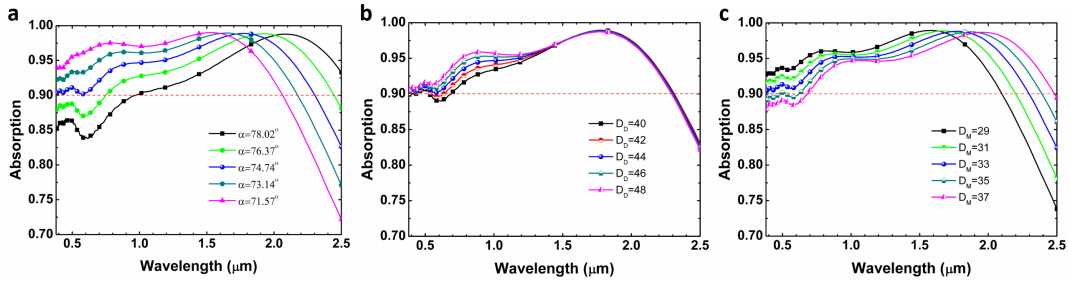

Figure 4.9: **Optimization process of VC. (a)** The impact of α when other parameters are $D_{\mathrm{M}} = 33nm, D_{\mathrm{D}} = 44nm$. **(b)** The impact of the thickness of the dielectric layer when other parameters are $D_{\mathrm{M}} = 33nm, \alpha = 74.74^o$. **(c)** The impact of the thickness of TiC layer when other parameters are $D_{\mathrm{D}} = 44nm, \alpha = 74.74^o$.

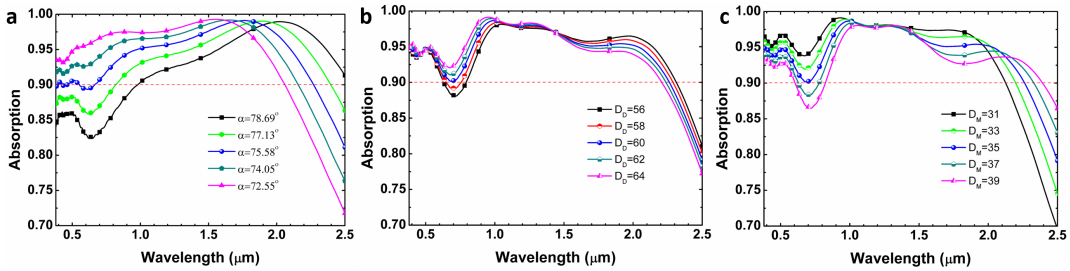

Figure 4.10: **Optimization process of TiN. (a)** The impact of α when other parameters are $D_{\mathrm{M}} = 35nm, D_{\mathrm{D}} = 60nm$. **(b)** The impact of the thickness of the dielectric layer when other parameters are $D_{\mathrm{M}} = 35nm, \alpha = 75.58^o$. **(c)** The impact of the thickness of TiC layer when other parameters are $D_{\mathrm{D}} = 60nm, \alpha = 75.58^o$.

others. As shown in Figure 4.8(b), D_D has a significant effect on absorption at shorter wavelengths but it is insignificant at longer wavelengths. To ensure absorption is always higher than 0.9, this geometry is selected as 44 nm. A higher value can be chosen to increase the absorption at the Vis region; however, this causes a reduction on the BW. As shown in Figure 4.8(c), absorption stays above 0.9 and has the widest spectrum when $D_M = 35nm$, which is the wavelength range of 380-2240 nm. Similar to TiC, the corresponding results for VC are shown in Figures 4.9(a-c). Its optimization process started with the parameters of $D_{\mathrm{M}} = 33nm, D_{\mathrm{D}} = 44nm, \alpha = 74.74^o$. The values of α and D_D keep the absorption sufficiently high from 0.9 and $D_M = 33nm$ provides the broadest

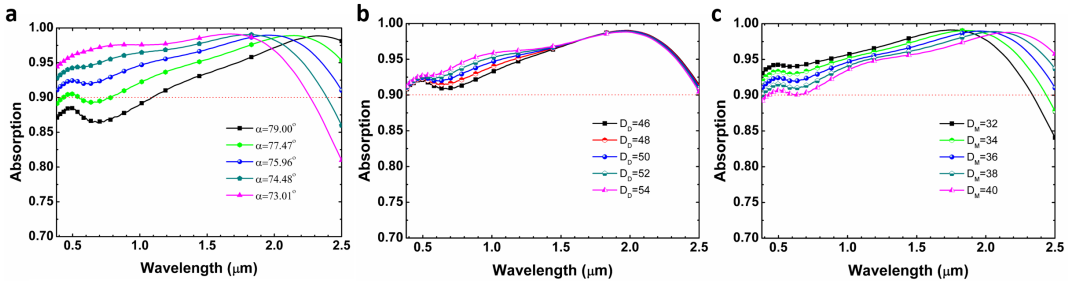

Figure 4.11: **Optimization process of VN. (a)** The impact of α when other parameters are $D_{\mathrm{M}} = 36nm, D_{\mathrm{D}} = 50nm$. **(b)** The impact of the thickness of the dielectric layer when other parameters are $D_{\mathrm{M}} = 36nm, \alpha = 75.96^o$. **(c)** The impact of the thickness of TiC layer when other parameters are $D_{\mathrm{D}} = 50nm, \alpha = 75.96^o$.

absorption spectrum. Therefore, the best performance is attained with these parameters in which absorption above 0.9 covers a range of 380-2290 nm.

In the case of TiN, the optimization process is shown in Figures 4.10(a-c). The starting values were $D_{\mathrm{M}} = 35nm, D_{\mathrm{D}} = 60nm, \alpha = 75.58^o$. Since absorption is not much below 0.9 at shorter wavelengths, α was not changed. To compensate for the dip that occurred around 700 nm wavelength, the dielectric thickness must be increased sufficiently. $D_D = 60$ nm is enough to keep absorption a little higher than 0.9. It can be increased to guarantee that it does not fall below 0.9; however, we kept it as 60 nm for the sake of broadest BW. Then, absorption above 0.9 in the wavelength range of 380-2265 nm is attained when $D_M = 35nm$. As demonstrated in Figures 4.11(a-c), VN performs superior light absorption than other TMC&TMN materials. For parameters of $D_{\mathrm{M}} = 36nm, D_{\mathrm{D}} = 50nm, \alpha = 75.96^o$, the designed structure has absorptivity above 0.9 in the wavelength range of 380-2500 nm, even more (we could not simulate longer wavelengths since we do not have refractive index data of the materials). Although VN is not a commonly used material, it is the only one that has such a performance with this design.

As the best performances of TMC&TMN materials are compared in Figure 4.12(a), VN shows the best performance (i.e., the broadest BW) in the trapezoidal array configuration among TMCs&TMNs. Furthermore, the type of the dielectric used in the design can also affect the absorption spectrum. Simulations were

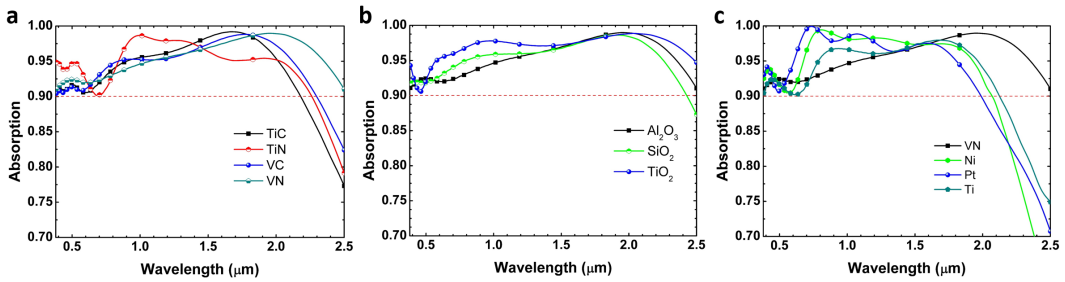

Figure 4.12: **Comparison of the best performances of TMCs,TMNs and metals. (a)** Comparison of the largest absorption spectrum attained with TMC (TiC, VC) and TMN (TiN, VN) materials. **(b)** The impact of the dielectric layer type on absorption when VN is used. **(c)** Comparison of the best performances of VN, Ti, Pt, and Ni.

repeated replacing Al_2O_3 with SiO_2 and TiO_2 and results are plotted in Figure 4.12(b) when VN is used. TiO_2 has more absorption strength and can have a longer spectrum if data of the materials would be available. Nevertheless, all three of them satisfy the valid wavelength range, which is 380-2500 nm.

To have a comprehensive study on the potential of these ceramic materials in the absorber design, the performance of the commonly used metals and VN should be compared. VN has higher melting point and resistance to oxidation and erosion compared to metals; however, its optical performance also has a crucial importance. Similar simulations were repeated to find the optimal geometries for each metal in trapezoidal array structure. As a result, while the optimal configuration of Ni with parameters of $D_{\mathrm{M}} = 32nm, D_{\mathrm{D}} = 54nm, \alpha = 72.65^o$ exhibits an absorption above 0.9 between 380-2070 nm, Pt with best parameters for the optimum absorption $D_{\mathrm{M}} = 32nm, D_{\mathrm{D}} = 50nm, \alpha = 71.03^o$ performs perfect absorption between 380-1990 nm and optimized Ti structure with parameters of $D_{\mathrm{M}} = 33nm, D_{\mathrm{D}} = 52nm, \alpha = 74.75^o$ shows perfect absorption in the wavelength range of 380-2125 nm. Therefore, VN performs better absorptivity than all lossy metals, as presented in Figure 4.12(c), besides being more durable to temperature and oxidation. That makes it a perfect candidate for high temperature broadband perfect absorber applications.

In order to understand how and where electromagnetic waves are absorbed

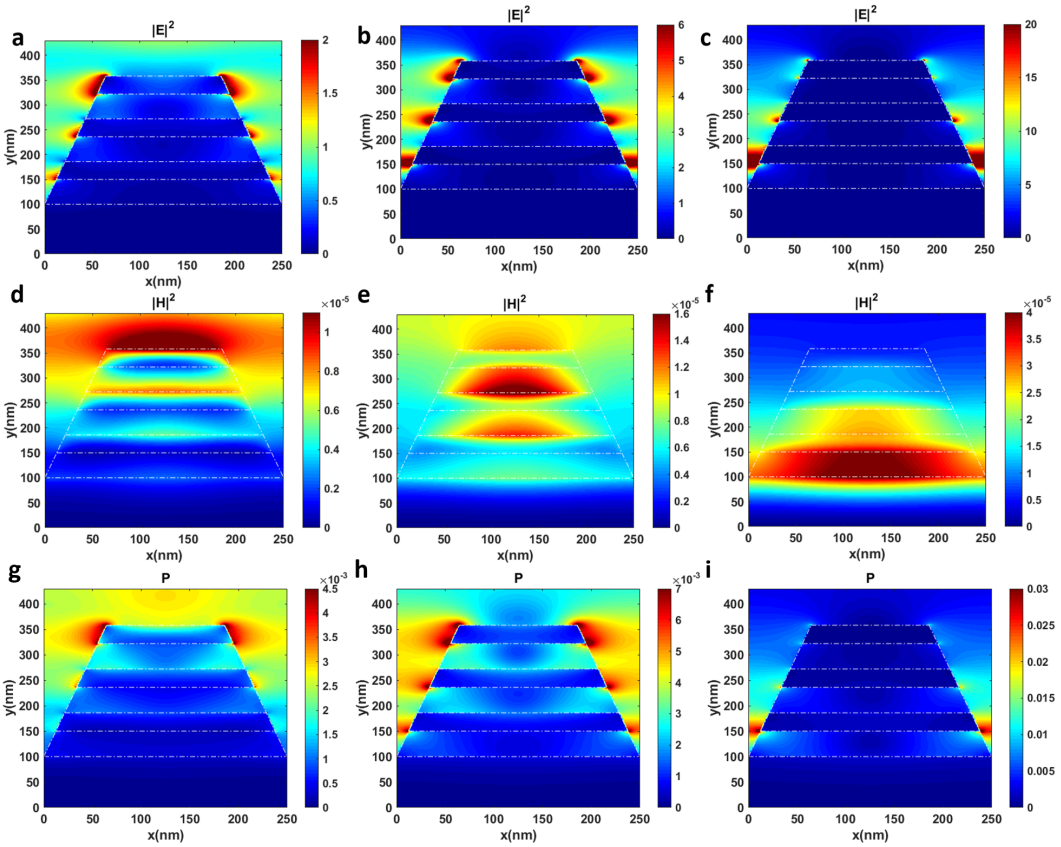

Figure 4.13: **Electric and Magnetic Field Distributions.** Magnitude square of E field distribution when **(a)** wavelength is 684 nm, **(b)** wavelength is 1350 nm, **(c)** wavelength is 2500 nm. Magnitude square of H field distribution when **(d)** wavelength is 684 nm, **(e)** wavelength is 1350 nm, **(f)** wavelength is 2500 nm. Absorbed power distribution when **(g)** wavelength is 684 nm, **(h)** wavelength is 1350 nm, **(i)** wavelength is 2500 nm.

by the designed perfect absorber, we examined the electric and magnetic field distributions and absorbed power profiles at several wavelengths throughout the absorption spectrum. Electric fields are mainly localized at the edges of metallic and dielectric layers and in the air gaps around metal, as shown in Figures 4.13(a-c). While the electric field is mostly localized near the top of the trapezoid at 684 nm wavelength, it is concentrated at each metal-dielectric cross-section and increased toward the bottom at 1350 nm, and it is mostly localized at the bottom of the trapezoid in the air gap when the wavelength is 2500 nm. As it is inferred from Figures 4.13(a-c), electric field strength is improved with longer wavelengths

and the localization region moves toward the bottom of the trapezoid. Contrary to the electric field, the magnetic field is localized between metallic layers, namely inside the dielectric, as shown in Figures 4.13(d-f). When the wavelength is 684 nm, the magnetic field is mainly localized in the air (just above the top metallic layer) and a part of it is localized at the boundary of dielectric and metal in the middle. Figures 4.13(e-f) demonstrate that the magnetic field is localized inside the structure in dielectrics as the wavelength becomes longer. Similar to the electric field, the magnetic field gets stronger and localized near the bottom of the structure as the wavelength becomes longer. Absorbed power at these three wavelengths, shown in Figures 4.13(g-i), reveals a confinement profile in parallel to fields. While electromagnetic waves with shorter wavelengths are absorbed by the top portion of the structure, longer wavelengths are absorbed with increasing strength at the air gaps between bottom parts of the trapezoids. Therefore, in this tapered design, in every wavelength range, the active region of the absorber changes. The superposition of these responses leads to such ultra-broadband light perfect absorption. We can deduce here that if the number of VN-Al_2O_3 pairs is increased, this structure can absorb even longer wavelengths.

Fabrication Considerations

Another important feature that should be considered in this design is its fabrication considerations. In this part, we will present some possible fabrication errors, their effects on the results and alternative solutions to compensate their negative effects and to obtain the same performance as mentioned before.

The first possible problem is difficulties in achieving adjacent trapezoids (with zero spacing) in a periodic fashion. The existence of a space may be unavoidable depending on the fabrication route used. The modified structure considering this factor and the resulting absorption spectrum are shown in Figures 4.14(a-b). Longer wavelengths cannot be absorbed perfectly anymore and absorption BW gets significantly narrower. This is due to the fact that a part of the incident light fully reflects from these spacing regions. To compensate for the disadvantage of

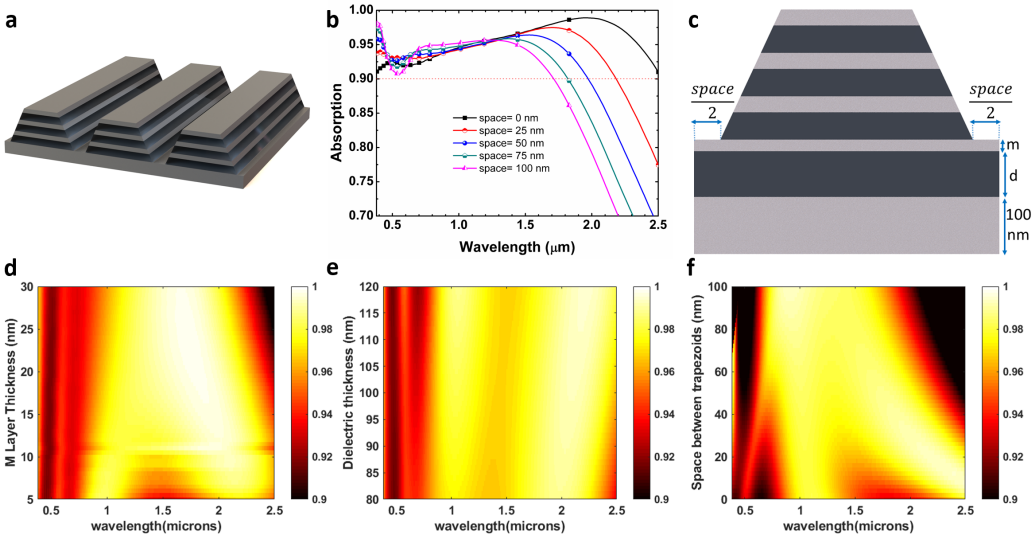

Figure 4.14: **Possible problems encountered in fabrication.** **(a)** The new 3D view of the structure if space is left between trapezoids. **(b)** Resulting absorption spectrum if space is left between trapezoids. **(c)** Proposed new design to compensate fabrication error and obtain the same result as before. **(d)** Optimization of m. **(e)** Optimization of d. **(f)** Absorption spectrum while space left between trapezoids is changed from 0 to 100 nm when the designed MDM is present under the trapezoidal structure.

fabrication feasibilities, we proposed a new design to replace the substrate with an MDM design which is composed of the same dielectric and material (i.e., Al_2O_3 and VN), as shown in Figure 4.14(c). The MDM layer was designed for the case when 50 nm space is left between the adjacent trapezoids. The optimization process of geometries of the MDM structure is shown in Figures 4.14(d-e). The bottom thick VN layer was chosen as 100 nm and the dielectric and thin VN layers were optimized one by one. At first, the dielectric layer was fixed to 100 nm and the thickness of the upper layer was swept from 5 nm to 30 nm. As shown in Figure 4.14(d), many of them result in absorption above 0.9, so we chose 10 nm to have the largest BW and tolerance to fabrication errors. Then, VN thickness was fixed to 10 nm and the dielectric thickness was swept from 80 nm to 120 nm. As shown in Figure 4.14(e), all of them again satisfy the requirements. Increasing the dielectric thickness gives a rise in absorption in longer wavelengths; however, causes fall in shorter wavelengths. To have a tolerance in both ways, we chose

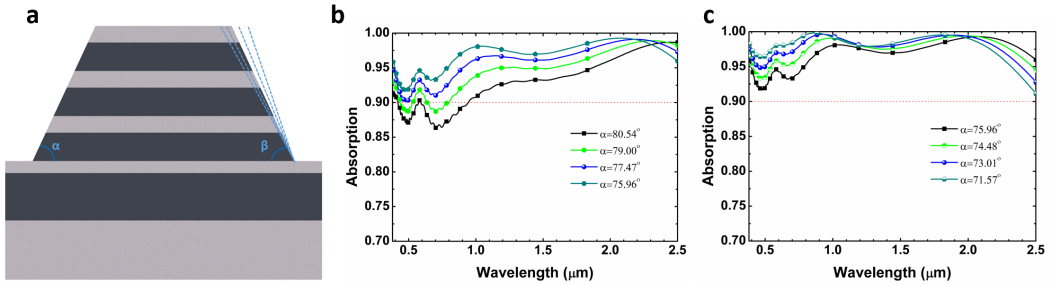

Figure 4.15: **Effect of side-wall angle error on absorption spectrum (a)** 2D view of the structure if one side-wall is not fabricated correctly. **(b)** Absorption spectrum if one side-wall is steeper than expected. **(c)** Absorption spectrum if one side-wall is less steep than expected.

a 100 nm thick dielectric layer. The resulting absorption spectrum of the design for different spaces between trapezoids is demonstrated in Figure 4.14(f). Thus, if the fabrication of designed ceramic-based trapezoidal array does not function as simulated due to fabrication limitations, adding a simple MDM layer increases its performance back into the desired levels or even better.

Side-wall angles of the trapezoid are hard to fabricate exactly as expected. Having tolerance for that is a precious property. We examined the effects of fabricating different side-wall angles on the absorption strength and spectrum. One of the side walls was drawn as planned in the optimal configuration, which is $\alpha = 75.96^o$ for VN, and the angle of the other wall was selected as higher and smaller values. In other words, the symmetric design of the trapezoids was distorted to an asymmetric one. The primitive shape of this error is shown in Figure 4.15(a). When one wall becomes steeper than optimal configuration, problems with shorter wavelengths occur, as shown in Figure 4.15(b). While the absorption strength is increased in the NIR region, it decreases below 0.9 in the visible region. When one side-wall angle becomes less than expected, while absorption in the visible region is increased, absorption at longer wavelengths decreases but still stays above 0.9, as shown in Figure 4.15(c). Therefore, the side wall angle has 2^o tolerance for bigger angles and 4^o tolerance for smaller angles when one wall is produced as planned. Even if the angle is distorted more, bigger or smaller, in both cases the absorption stays above 0.85.

Chapter 5

Simultaneous Realization of Visible and Near-infrared Ultra-broadband Absorber and Ultra-High Sensitive Mid-infrared Refractive Index Sensor Using Lithography-Free Random Bismuth Nanostructures

This chapter is based on the submission "Simultaneous Realization of Visible and Near-infrared Ultra-broadband Absorber and Ultra-High Sensitive Mid-infrared Refractive Index Sensor Using Lithography-Free Random Bismuth Nanostructures" to Advanced Optical Materials journal of Wiley.

5.1 Preface to Broadband and Narrowband Perfect Absorber Designs

As explained in "Preface to Broadband Perfect Absorber Designs" section of Chapter 4, metamaterials, which have exotic properties that cannot be observed in natural materials, are of great interest in designing high performance light absorbers utilizing subwavelength geometries and designs. Many application areas such as sensing [42], spectroscopy [43], photovoltaic [22], thermal photovoltaic [24] and photodetection [44] require high performance perfect absorbers. For this purpose, several designs were developed in various shapes, sizes and architectures to attain narrowband and broadband perfect absorbers. Landy et al. proposed perfect absorber based on a metallic split ring resonator [13]. Wen et al. improved the absorption profile of this design [89]; however, their proposed designs were limited to a narrow operating wavelength, absorbing a small fraction of the solar irradiation due to lack of any trapping mechanism. Light confinement inside the structure was achieved introducing a new architecture which is MIM cavity design. This configuration is based on the cancellation of upward and downward moving lights between two metallic layers. Aydin et al. designed an MIM structure whose top layer was comprised of crossed trapezoid array with subwavelength thickness, and attained average 0.71 absorption in the range of 400 nm-700 nm [55]. In the light of this work, many broadband perfect light absorbers with larger bandwidth and stronger absorptivity were designed by changing the top layer pattern and structure geometries. Nanodiscs [46, 90, 60, 54], nanorings [61] and nanopatches [57, 58, 50, 59] are some examples of choices as top layer pattern in the literature. However, these designs have a complex fabrication route and they are not large scale compatible, because they require EBL for realization of the top nano unit layer. Mattiucci et al. theoretically and experimentally proved that planar MI pairs can be used to obtain ultra-broadband perfect light absorber, and adding new MI-pair extends the absorption spectrum toward longer wavelengths [63]. Many multilayer planar structures were designed and fabricated using this fact [65, 53, 91, 92]. Ghobadi et al. proposed a planar two MI-pair structure composed of Pt and Al_2O_3 which yields absorption above

0.9 in the range of 400 nm-1490 nm [64]. Although this architecture provides lithography-free fabrication route and broadband response, the absorbed power is not accessible due to being confined mostly in the middle metallic layer. Also, depositions require high precision because 1-2 nm changes in the thickness of the metallic layer have a significant effect on the absorption performance.

Recent studies demonstrated that randomly distributed and disordered structures can have on par performance with periodically ordered structures [93, 94, 95, 96, 97, 98, 99, 100], or even surpass them. Hedayati et al. proposed an MIM structure whose top metallic layer is neither planar nor patterned layer but randomly distributed nanocomposites. A black sample with broadband perfect absorption above 0.9 in the range of 400 nm-700 nm was attained experimentally [101]. They also produced the first broadband perfect absorber by using copper (Cu) and nanocomposites made of Cu utilizing sputtering and evaporation techniques which has absorption above 0.9 in the range of 300 nm - 700 nm [102]. Although fabrication process of this work is straightforward, BW of the absorber is significantly limited. Ghobadi et al. demonstrated an ultra-broadband perfect absorber which has absorption 0.97 on average in the range of 300 nm-1100 nm using randomly oriented and densely packed dielectric scaffold metallic nanowires fabricated using chemical vapor deposition (CVD) technique [64]. Bae et al. designed a flexible thin-film black gold triangular prism coated around dielectric scaffold to attain absorption above 0.9 in the range from 400 nm to 2500 nm [103]. Chemical processes such as wet etching is utilized to widen the pores and to extract periodically distributed dielectric triangular prisms at desired geometries by controlling the etching time and temperature; however, fabrication of these kind of structures are challenging because all fabrication parameters have to be adjusted precisely during the entire process [104, 105]. As an alternative to chemical processes, Jen et al. used oblique-angle deposition approach with e-beam evaporation technique to fabricate densely packed Al - silver (Ag) nanohelices [106]. Although they attained absorption above 0.8 in the range of 400 nm-2000 nm, their fabrication includes many steps and complexity due to controlling many parameters, such as substrate spin rates, radius of curvatures, pitch lengths.

On the other hand, some studies intend to design narrowband absorbers which have an absorption peak at single resonance wavelength, contrary to broadband absorbers. Many different nanopattern configurations were employed for achieving high-sensitivity narrowband absorbers [45, 107, 108, 109, 110, 111, 112, 113, 114, 115, 116, 117]. Liu et al. designed an MIM nanodisc narrowband perfect absorber with sensitivity of 400 nm/refractive index unit (RIU) [45]. They also developed a planar metamaterial which has cut-out structures in a thin gold film as analogue of an optically bright dipole antenna and an optically dark quadrupole antenna [107]. This metamaterial sensor based on coupling effects experimentally yields a sensitivity of 588 nm/RIU. Lee et al. designed a $7x7$ gold nanoslit arrays on a glass substrate which demonstrates sensitivity of 668 nm/RIU [110]. Di Meo et al. designed a polarization insensitive cross-shaped plasmonic nanoantennas based chemical sensor with a sensitivity of 600 nm/RIU [111]. Yong et al. theoretically proposed a unit-cell with four very close cylindrical nanodiscs MM architecture which can operate as a refractive index sensor with a sensitivity of 885 nm/RIU [112]. Pang et al. designed a nanohole array surface plasmon resonance (SPR) biosensor which can reach to 1520 nm/RIU sensitivity for certain cases [113]. Jin et al. demonstrated a highly sensitive integrated optical biosensor based on two cascaded micro-rings resonator with sensitivity of 1300 nm/RIU [114].

5.2 Motivation and Novelty

In this work, we propose a facile fabrication route to realize single Bismuth (Bi) metal nanostructure based, lithography-free double functional design which has ultra-broadband absorption in the Vis and NIR regimes, and narrowband absorption in MIR regime. The designed structure is a metal-metal (MM) configuration, which comprises of a thick planar bottom layer to ensure zero transmission and a layer of disordered and densely packed nanorods. We utilize FDTD method to investigate the impact of parameters on the absorption spectra of the design, light confinement mechanism inside the structure and superiority of Bi over other metals. To explain compatibility of Bi to broadband absorber designs, a systematic

modeling approach is conducted. TMM is carried out to find the ideal permittivity region of the top layer upon a thick metallic substrate for perfect absorption, and Bruggeman's EMT is used to predict the effective permittivity of the metal nanorod-air composition for different metals such as Ni, Cr, gold (Au), tungsten (W) and Bi. It is shown that extraordinary optical properties of Bi provides perfect absorption with the widest BW in Vis and NIR ranges. A simple and lithography-free fabrication route is followed using thermal evaporator technique. Oblique-angle deposition approach is utilized to produce disordered and densely packed nanorods using the self-shadowing effect of primarily grown nanorods. We experimentally show that the proposed device achieves broadband absorption nearly above 0.8 in Vis and NIR, and narrowband absorption resonance at 6.54 μm in MIR. To utilize narrowband response for sensing applications, we spin coated poly(methyl methacrylate) (PMMA950K) onto the surface of the structure, and observed 1.05 μm red shift in resonance wavelength which results in an ultra-high experimental sensitivity of 2.151 μm/RIU. Overall, we unveil a new material (i.e., Bi) for strong light-matter interaction based applications, whose superiority is proven theoretically and by simulations, and fabricated a highly sensitive sensor in MIR besides having ultra-broadband absorption in Vis and NIR regimes.

5.3 Results and Discussion

5.3.1 Numerical Simulations

Randomly distributed nanorods cannot be exactly modeled in simulation region due to imperfect shape of the fabricated nanorods and unpredictable surface roughness. However, to better understand the impact of the parameters on absorption performance and to reveal trend, numerical simulations were conducted for a simplified version of the fabricated sample using the commercial Lumerical FDTD Solutions software package. Details of the simulation setup are outlined in the experimental section. The main parameters that affect the absorption

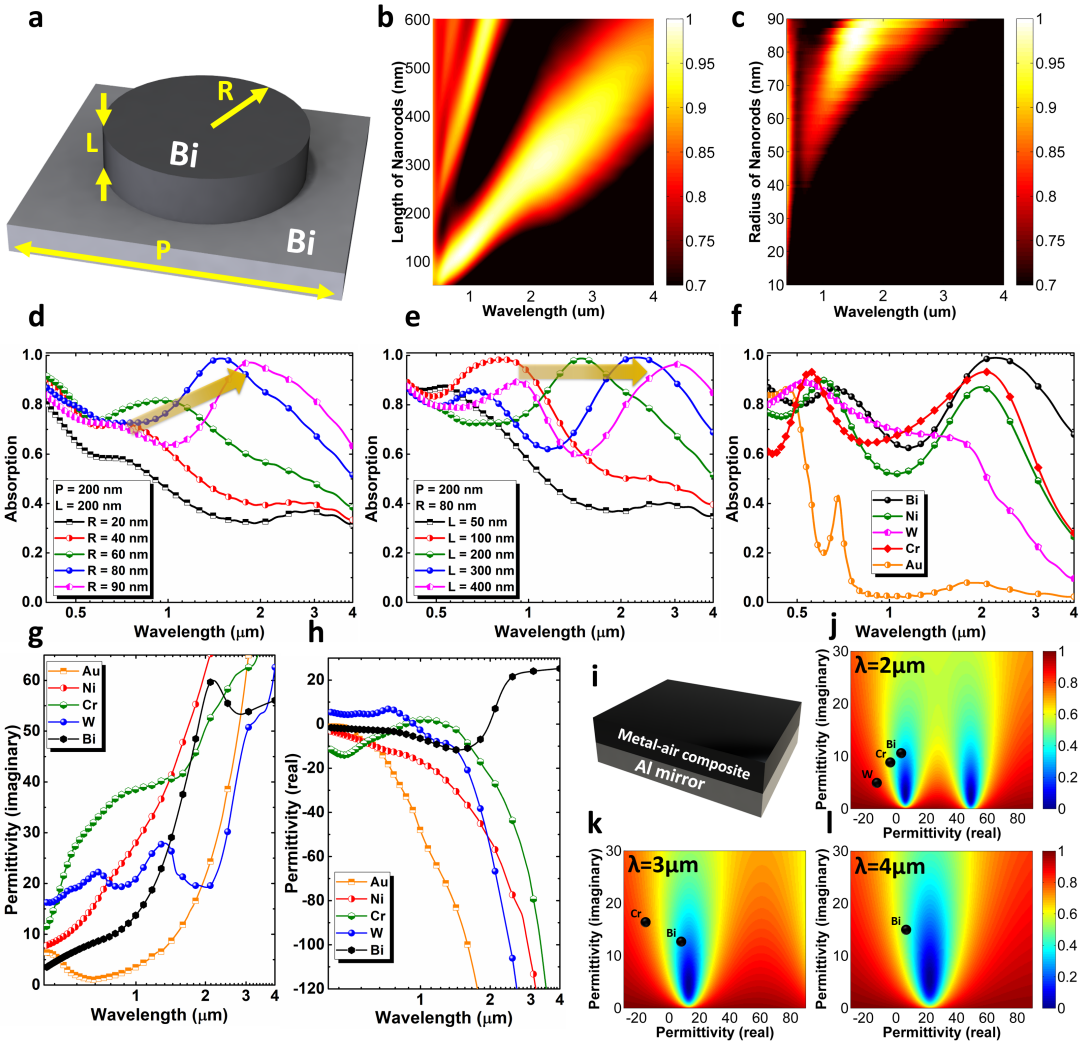

Figure 5.1: **Parameter effect and Modelling.** **(a)** The perspective view of the designed 2-layer structure. **(b)** Contour plot of absorption for length parameter. **(c)** Contour plot of absorption for radius parameter. **(d)** Sweep and optimization of R from 20 nm to 90 nm while $P = 200nm$ and $L = 200nm$. **(e)** Sweep and optimization of L from 50 nm to 400 nm while $P = 200nm$ and $R = 80nm$. **(f)** Absorption performance comparison of Bi with Au, Cr, Ni and W in FDTD simulations. **(g)** Real and **(h)** imaginary part of the permittivity of the given materials. **(i)** Generalized case of designed MM structure with a thick Al layer as a common reflector and an effective medium of metal nanorod-air composition. Contour plot of reflection of the structure **(i)** and effective permittivity of the upper layer as a dot at the wavelengths of **(j)** $\lambda = 2\mu m$, **(k)** $\lambda = 3\mu m$, **(l)** $\lambda = 4\mu m$.

spectrum are radius (R) and length (L) of the nanorods and period (P) of the unit cell, in other words, packing density of the structure. These parameters are shown on Figure 5.1(a). In this design, the incident light interacted with metallic nanorods is diffracted into the metal nanorod-air composition and excites several modes. These are mainly the longitudinal resonant modes among the nanorods because it is known that metallic nanostructures elongated at one direction can support multiple longitudinal and transverse modes [64] which are mainly localized surface plasmon resonances (LSPRs). In that structure, a nanorod can be considered as a monopole antenna where SPRs are excited at the Bi-air interface. To gain an insight on the influence of different geometries on the absorption response of the aforementioned MM design, the contour plots have been extracted for L and R. As Figure 5.1(b) clearly implies, the proposed nanoantenna has multiple longitudinal modes that appear as straight lines. For $L < 200nm$, only the dominant mode is excited (which is the first order longitudinal mode) and near unity absorption is acquired in a narrow spectral range. As the rod length becomes larger, multiple absorption modes are supported with design and superposition of these modes leads to a broadband near unity absorption. These results are in line with the previous findings [64]. Another prominent factor is the rod's transverse dimension which is R. For this plot, the L is fixed at 200 nm and P is 200 nm. As it can be clearly seen from Figure 5.1(c) panel, for small radii, light absorption capability of the MM design is poor. However, as we increase this geometrical parameter, the absorption gets stronger and its spectral bandwidth is broadened. In fact, in small radius values, the coupling between neighborhood nanorods is weak and therefore the overall response of the structure is dominated by the bottom reflecting flat layer. As the radius increases, the gap between nanorods gets smaller, and consequently stronger light confinement is achieved. It should be noted that R and packing density are relevant with each other while period is constant because as radius is increased, nanorods get closer and become more densely packed. This strong field localization, coupled with lossy nature of Bi metal, will lead to perfect light harvesting in a broadband wavelength regime. To have a closer view on these data, cross section views have been extracted from these panels and depicted in Fig 5.1(d-e). Figure 5.1(d) demonstrates resonance modes for different radius values where the longer wavelength resonances belong

to initially excited (lower order) modes. When nanorods have small radius, absorption performance is significantly poor because of the low packing density. In fact, the response is mainly originated from the bulk absorption of Bi bottom plate. As the radius increases (or correspondingly the gap reduces), the dominant peak becomes stronger and shifts to longer wavelength values. According to previous studies, the light confinement in deep sub wavelength nanogaps can cause a spectrally narrow light absorption [118]. As the gap reduces, this absorption peak experiences a red shift. This is in line with our findings. However, the story is quite different in the shorter wavelengths. The high packing density will turn this nanostructure design into a semi mirror bulky structure and thus, the absorption in shorter wavelengths will be diminished. Therefore, a wise design should have multiple gap sizes to cover both spectral regions. To find an optimum cursor, we preferred to choose the largest bandwidth with at least 0.7 absorption to have satisfying absorptive properties in Vis and NIR regions; therefore, we continued to simulations with the radius of 80 nm. The impact of L on the absorption was analyzed in a similar fashion where R and P were fixed at 80 nm and 200 nm, respectively. Similar to absorption profile for different radius values, absorption spectrum is comprised of superposed multiple resonance modes, as shown in Figure 5.1(e). Contrary to radius dependence, absorption strength gets stronger continuously with increasing nanorod lengths as expected because the excited modes are mainly longitudinal modes, and new modes are excited with increased nanorod lengths. Similar to the effect of R, a slight red shift of resonance wavelengths is occurred in longer nanorods. It is clearly seen from Figure 5.1(e) that lower order modes (resonances at longer wavelengths) have weaker absorption peaks at resonances than higher order modes (resonances at shorter wavelengths) because as the order of modes is increased, modes get closer and coupling between them becomes stronger. Absorption profiles of different modes are merged, and therefore, absorption approaches to unity. Looking at these data, the optimal L value was chosen as 300 nm to have a fair trade-off between absorption amplitude and bandwidth.

As demonstrated by these results, this Bi based MM structure has quite strong absorption response. However, it is quite challenging to obtain a broadband

perfect absorber with an MM structure since metals are reflective due to their high refractive index at Vis and infrared regimes. The reason of getting this strong absorption with such a simple structure is definitely due to the excellent optical properties of Bi. To compare this metal with other common metals, the absorption of the MM structure was extracted in the abovementioned optimal dimensions. Figure 5.1(f) reveals the superior absorption performance of Bi in comparison with the metals such as Cr, Ni, W (as lossy metals) and Au (as nobel metal) when they are all simulated with identical designed MM structure. While these materials, except Au, show similar absorption spectrum up to 2 μm, Bi maintains its performance in NIR and MIR region, though absorption of the other metals decreases abruptly to the 0.3 levels. Such a different absorption performance arises from the unique optical property (i.e., permittivity) of Bi. Although Bi and other metals do not have significant differences in terms of the imaginary part of their corresponding permittivities, see Figure 5.1(g), real part of the permittivity of Bi presents a completely different dependence on the wavelength as seen in Figure 5.1(h). Bi and other metals have permittivities whose real parts have values close to each other up to 2 μm, like in the absorption performance in Figure 5.1(f). However, real part of the permittivities of other metals abruptly decreases to huge negative values after 2 μm while real part of the permittivity of Bi takes positive values, which is a unique feature that belongs to Bi. In fact, Bi acts as a plasmonic metal in shorter wavelengths and a lossy dielectric in longer wavelengths.

To demonstrate the importance of having positive values of real part of the permittivity for design of broadband absorbers, we conducted a systematic study to predict the absorption performance of different materials in the designed MM structure. We generalized the problem in theoretical modeling by using a thick Al layer as a commonly used perfect mirror in the bottom layer and a composition of metallic nanorods and air in the top layer, as shown in Figure 5.1(i). We first adopted a modeling approach to find the ideal material for metal-air composite in which the overall reflection from the structure is zero. TMM was carried out to find the total reflection from the design. The generalized case of TMM, described in chapter 2, was adapted to a 2-layer MM design. For TM polarization, H_{y} in

that structure becomes that

$$H_y(z) = \left\{ \begin{array}{cc} A_i e^{ik_A z} + A_r e^{-ik_A z}, & z <= 0 \\ M_1 e^{ik_C z} + M_2 e^{-ik_C z}, & 0 < z <= L \\ C_1 e^{ik_M (z-L)} + C_2 e^{-ik_M (z-L)}, & L < z <= L + D_M \\ A_t e^{ik_A [z-(D_M+L)]}, & z > L + D_M \end{array} \right\} \quad (1)$$

where A_i, M_1, C_1 and A_t are coefficients of the propagating waves in $+z$ direction and A_r, M_2 and C_2 are coefficients of the propagating waves in $-z$ direction in media of air, metallic substrate and metal nanorod-air composition, respectively. D_M and L are the thicknesses of the bottom thick planar metallic layer and upper metal nanorod-air composition layer. k_A, k_C and k_M are propagation constants in air, metal nanorod-air composition and metallic substrate, respectively. Applying the appropriate boundary conditions, reflection of the incident light from the structure can be obtained as $R = |\frac{F_{11}}{F_{12}}|^2$. Here, $F = \begin{bmatrix} F_{11} \\ F_{12} \end{bmatrix} = a_1^{-1} m_{11} m_{12}^{-1} m_{21} m_{22}^{-1} a_2$ where

$$a_1 = \begin{bmatrix} 1 & 1 \\ \frac{ik_A}{\epsilon_A} & \frac{-ik_A}{\epsilon_A} \end{bmatrix}, a_2 = \begin{bmatrix} 1 \\ \frac{ik_A}{\epsilon_A} \end{bmatrix} \quad (2.a)$$

$$m_{11} = \begin{bmatrix} 1 & 1 \\ \frac{ik_M}{\epsilon_M} & \frac{-ik_M}{\epsilon_M} \end{bmatrix}, m_{12} = \begin{bmatrix} e^{ik_M D_M} & e^{-ik_M D_M} \\ \frac{ik_M e^{ik_M D_M}}{\epsilon_M} & \frac{-ik_M e^{-ik_M D_M}}{\epsilon_M} \end{bmatrix} \quad (2.c)$$

$$m_{21} = \begin{bmatrix} 1 & 1 \\ \frac{ik_C}{\epsilon_C} & \frac{-ik_C}{\epsilon_C} \end{bmatrix}, m_{22} = \begin{bmatrix} e^{ik_C L} & e^{-ik_C L} \\ \frac{ik_C e^{ik_C L}}{\epsilon_C} & \frac{-ik_C e^{-ik_C L}}{\epsilon_C} \end{bmatrix} \quad (2.b)$$

and $k_{i=(A,C,M)} = \sqrt{\frac{\epsilon_i \omega^2}{c^2} - k_x^2}$ where c is the speed of light, k_x is the propagation constant in the x-direction, and ϵ_A, ϵ_M and ϵ_C represent permittivity of air, metallic substrate (i.e., Bi) and metal nanorod-air composition, respectively. By this method, we can obtain the contour plot of reflection depending on real and imaginary parts of the permittivity of metal-air composite at a specific wavelength as

shown in Figure 5.1(j-l). In other words, we can replace the metallic nanodiscs with an effective medium which is made of metal and air fillings. Thus, one can determine the overall reflection from the whole structure by looking at where effective permittivity of the upper layer falls on this plot. Therefore, we need to know the effective permittivity of the metal-air composite medium to complete the modeling of the designed structure. For this purpose, we carried out Bruggeman's EMT to predict the effective permittivity ϵ_{eff} of the metal nanorods-air composition. It should be noted that this model is accurate if dimensions are much smaller than the wavelength. However, our main goal is to get an insight on the differences between various metals, rather than having an accurate modeling result. Based on the Bruggeman's theory, ϵ_{eff} is calculated according to the formula of

$$\epsilon_{eff} = \frac{1}{4}((3f_1 - 1)\epsilon_1 + (3f_2 - 1)\epsilon_2 \pm \sqrt{((3f_1 - 1)\epsilon_1 + (3f_2 - 1)\epsilon_2)^2 + 8\epsilon_1\epsilon_2}$$

where f_1 and f_2 are filling factors of metal nanorods and air, ϵ_1 and ϵ_2 are permittivity of Bi and air, respectively. The sign of the square root is chosen in a way that the imaginary part of the effective permittivity is positive due to causality in any passive medium. The permittivity data of Bi was extracted using J.A. Woollam Co. Inc. V-VASE and IR-VASE ellipsometer in the wavelength range of 0.3 μm to 10 μm, and permittivities of Au, Cr, W and Ni were taken from Lumerical FDTD Solutions database. The calculated effective permittivity values for all these materials are projected onto the reflection contour plots in Figure 5.1(j-l). In these figures, the blue semi-circles are permittivity values that lead to a reflection below 0.3 (or equivalently an absorption above 0.7). At 2 μm incident light wavelength, Bi and Cr are located in the vicinity of this ideal circle. However, as we go to longer wavelengths, these blue regions shift to real part of the permittivity values larger than unity. Thus, any composition of a metal (with a permittivity that has a negative real part) and air (whose permittivity is one) cannot satisfy this ideal condition. However, Bi, with a permittivity that has a positive real part, can satisfy this matching condition upon finding the proper disc dimensions. This reveals the unique property of the Bi layer on achieving ultra-broadband light absorption in an MM design configuration. Effective permittivity of Bi nanorods-air composition takes a value between permittivity of Bi and air (1

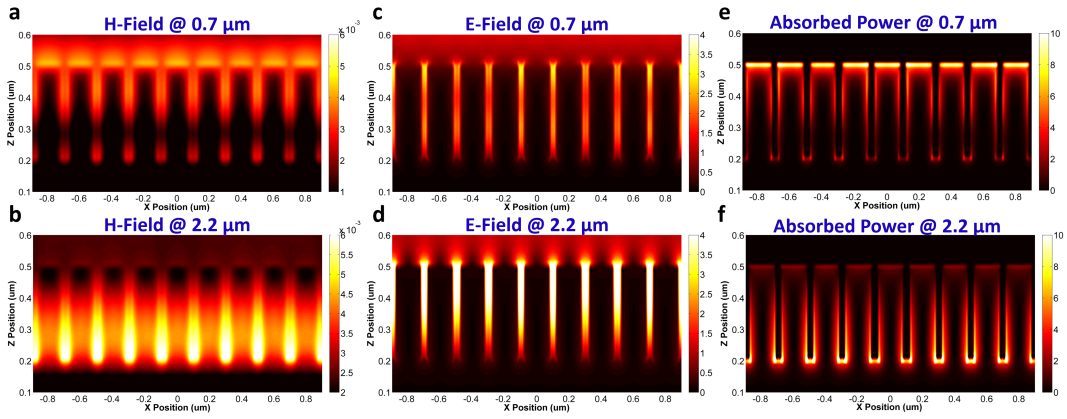

Figure 5.2: **Field Profiles** H-field profiles at **(a)** 0.7 μm and **(b)** 2.2 μm. E-field profiles at **(c)** 0.7 μm and **(d)** 2.2 μm. Absorbed power profiles at **(e)** 0.7 μm and **(f)** 2.2 μm.

for real part and 0 for imaginary part) depending on filling fraction of materials. In these plots, f_1 was chosen as $f_1 = \frac{\pi R^2}{P^2} = 0.503$ for $R = 80nm, P = 200nm$. At 2 μm incident light wavelength, only effective permittivity of Bi is located in the vicinity of perfect absorption circle.

To better understand the excited modes nature and how light is confined inside the nanorods at the resonance wavelength, E-field, H-field, and absorbed power graphs are shown in Figure 5.2(a-f) at two different wavelengths of 0.7 and 2.2 μm which are the positions of absorption peaks. When the structure is considered from a monopole antenna standpoint, multiple SPPs at different wavelengths are excited at the Bi-air interface. The excited resonant plasmon modes confine the H-field of the incident light mostly at the top of the nanorods at shorter wavelengths depending on the order of the modes. At Vis region, material properties become dominant factor on determining the overall reflection from the structure. Near-ideal index matching between Bi nanorods-air composition and the environment (i.e., air) results absorption at the interfaces. At longer wavelengths, small gaps between adjacent nanorods result in stronger field localization due to the interaction between metallic nanostructures [118]. Thus, incident H-field is mostly confined at the bottom of the nanorods and very small gaps, as shown in Figure 5.2(a-b). E-field is mainly localized at the gaps along the nanorods, as

shown in Figure 5.2(c-d). When we plotted absorbed power at these two wavelengths, it is apparently seen that light is mostly confined at the top edges of the nanorods at 0.7 μm while absorbed power is localized around the side-walls at the bottom of the nanorods at 2.2 μm, see Figure 5.2(e-f). Light confinement region is slipped into the bottom parts of the nanorods and gets stronger with increasing wavelength. It can be inferred from the analogy between H-field and absorbed power localization regions that the structure exhibits magnetic dipole characteristics.

Our discussions up to this point have demonstrated the extraordinary absorption response of Bi metal. It was demonstrated that a strong absorption can be acquired in a periodic pattern of Bi nanostructures in an MM configuration. Substantial improvement can be accomplished by introducing a randomness into the geometries of the design. It was shown that the change in L and R can be employed to manipulate the spectral position of the absorption peak. This randomness is not only applied into design parameters but also it can be used in the nanorods orientation. In such a design architecture, multiple absorption peaks can be superposed to achieve the overall perfect absorption throughout an ultra-broadband wavelength regime. Therefore, we carried out simulations by randomizing the nanorods. For this purpose, we designed a unit cell containing 16-nanorods with random design geometries. Using random number generator function of the Lumerical software, nanorods were rotated both around x-axis and y-axis at a random degree between -30 and 30. We also added 10% tolerance to the radius and length of the nanorods (R can take a value between 72 and 88 while L can take a value within 270 and 330). Using this approach, the absorption profiles of four different random combinations were compared with a periodic design, as shown in Figure 5.3(a). As this figure clearly highlights, when the structure has such random geometries, it achieves broader and stronger absorption compared to the periodic structure. Also, different randomness scenarios reveal distinct absorption spectra in which the minimum may differ with a value around 0.1 (while random case 1 has minimum absorption around 0.68, random case 4 reveals minimum absorption around 0.78). The simulated random 16-nanorod unit cell is eventually a periodic structure; however, the fabricated

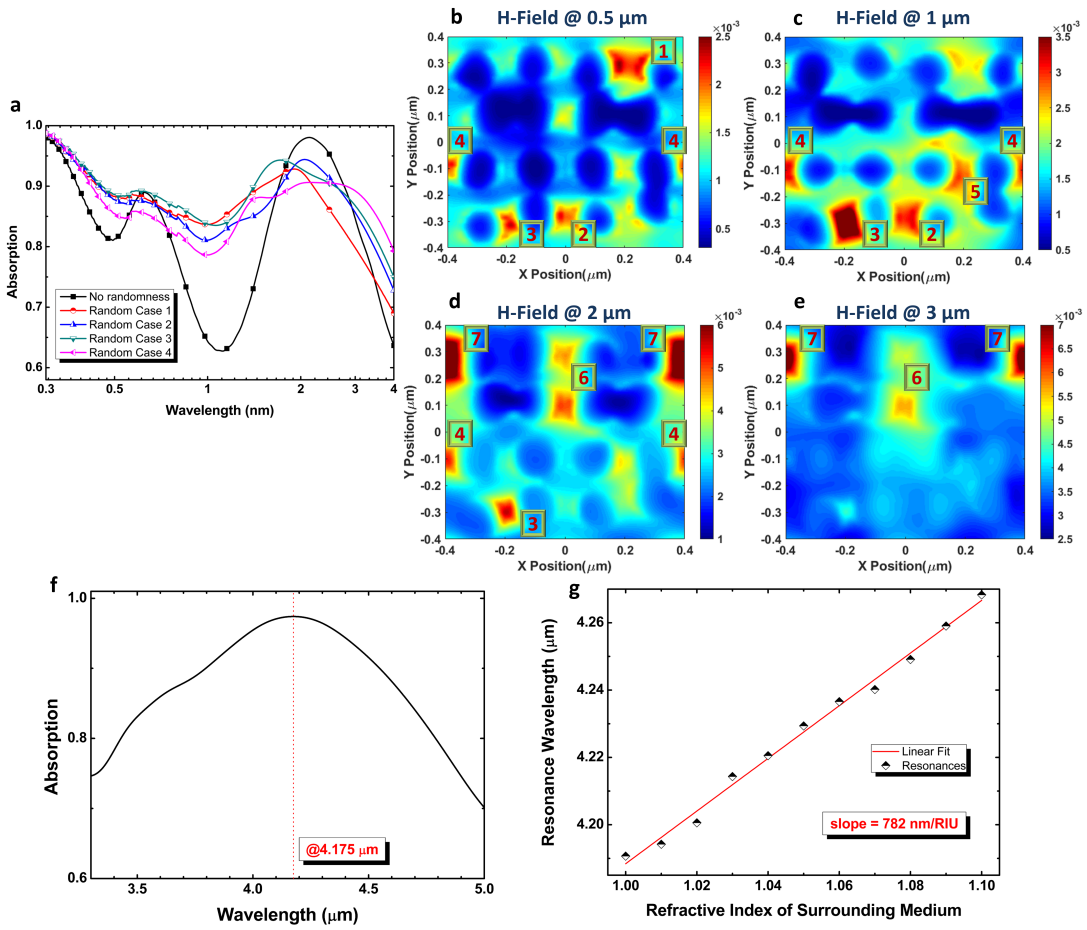

Figure 5.3: **Effect of randomness on absorption performance and light confinement mechanism.** **(a)** Absorption spectra of 16-nanorods unit cell when nanorods have no orientation and different random scenarios. H-field profile of the unit cell at the middle height of the nanorods at wavelengths of **(b)** 0.5 μm, **(c)** 1 μm, **(d)** 2 μm, **(e)** 3 μm. **(f)** Simulated absorption spectrum for the range of 3.2 to 5 μm. **(g)** Resonance wavelengths for changing surrounding medium refractive index values and linear fit in order to find sensitivity of the sensor.

sample simultaneously includes many different combinations of randomly grown nanorods. Thus, simultaneous utilization of optical response of Bi and the proposed randomness can lead to a flat perfect absorption in an ultrabroadband range. To better explain this, H-field profiles of the unit cell comprised of 16 random nanorods are shown in Figure 5.3(b-e), on which localized light confinement regions are numbered. It can be inferred from these panels that at four different wavelengths, there is a circulation of resonance regions so that at least one mode is excited in the structure. In other words, the active regions of the MM structure are interchanged in different wavelength values. For example, incident light with 0.5 μm wavelength excites four different modes in the unit cell, where 1 is the strongest light confinement region. At 1 μm, resonant mode at 1 vanishes and a new mode is excited at 5 while the light is mostly confined at region 3, see Figure 5.3(c). At 2 μm, the new resonant modes are excited at regions 6 and 7 instead of modes at regions 2 and 5. We can conclude from these field profiles that the proposed random structure can support multiple modes in different wavelength values. Thus, there are always excited resonance modes in the structure; and this in turn leads to a broadband absorption of the incident light.

In addition to broadband absorption profile of the proposed design in Vis and NIR, MIR response of the periodic and perpendicular Bi nanorods was analyzed, and a narrow plasmonic resonance peak was also noted at 4.175 μm by simulations, as shown in Figure 5.3(f). In plasmonic narrowband absorbers [101, 102, 64, 103, 104, 105], where the absorption is achieved via excitation of SPR in the metal-dielectric interface, the change in the index of the surrounding medium can cause a shift in the absorption peak. This red shift of the resonance, induced by the refractive index increase, is widely utilized for sensing applications. The sensing capability of a design is usually described by the term of sensitivity, which is defined as $S = \frac{\Delta\lambda}{\Delta n}$ where S, $\Delta\lambda$ and Δn are sensitivity, shift in resonance wavelength and change in refractive index of the surrounding medium on the surface, respectively. To demonstrate the sensing performance of this design, refractive index of the environment was varied from 1 to 1.10 with a step interval of 0.01, and the corresponding new resonance wavelengths are shown in Figure 5.3(g), where obvious red shift of resonance is observed. The sensitivity

is measured from the slope of the line that is attained by linearly fitting the peak spectral positions of the resonances. It is calculated as 782 nm/RIU, which is on par with the other reported values.

5.3.2 Fabrication

Although the oblique-angle deposition method is commonly used to fabricate sidewall coatings of the edges or gratings [119, 120, 121, 122], this paper proposes to use this method to fabricate disordered and densely packed nanorods utilizing self-shadowing effect of the primarily grown nanoislands. Samples have been fabricated using the thermal evaporator equipment in two steps. In the first step, a simple thick planar Bi layer was coated on a silicon (Si) wafer to constitute the basement for nanorods and to act as a back reflecting mirror. On the second step, shadowing effect of the primarily grown nanorods were exploited and desired structure was realized using oblique-angle deposition. As illustrated in Figure 5.4(a), sample was positioned at a few degrees incline with respect to the vertical axis; therefore, coating was realized with a bottom-up approach. Although evaporated gas molecules are grown in every part of the sample at the beginning of the evaporation process, as the deposition continues, initially grown nanorods prevent the nanostructures behind them to be grown due to shadowing effect. At the early steps of the coating, nanoislands of short Bi nanorods came into existence with a random distribution, as demonstrated in the SEM image of the fabricated sample in Figure 5.4(a). As the evaporation continued, nanoislands were elongated in one direction and densely packed Bi nanorods emerged, as shown in the cross sectional view of the Bi nanorods in Figure 5.4(b). It should be noted that elongated nanorods are separated by small gap distances and they preserve their shape though increasing evaporation time. The proposed route is a large scale compatible and facial approach to fabricate randomly distributed nanorods with high packing density using a straightforward deposition step. Moreover, the length of the nanorods can be adjusted by controlling the evaporation time. The details of the fabrication route are given in the Experimental section.

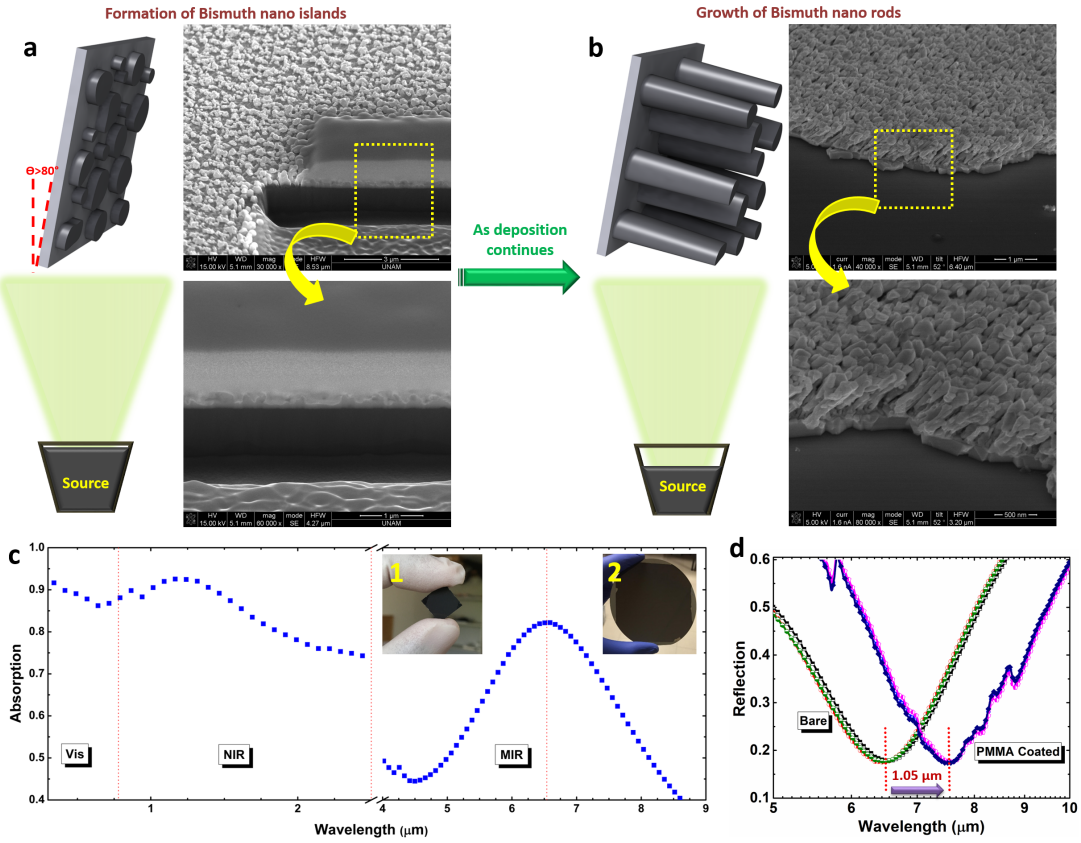

Figure 5.4: **Fabrication and characterization results (a)** Early steps of angled deposition technique to create Bi nanoislands. **(b)** Transformation of nanoislands into the nanorods as deposition continues. **(c)** Absorption spectra in all regions (Vis, NIR and MIR) of the fabricated sample. **(d)** Narrowband absorption of the Bare and PMMA coated samples, and the associated spectral shift of resonance for refractive index sensing. The insets 1 and 2 of **(c)** show the fabricated small-area sample and 4-inch Silicon wafer, respectively.

5.3.3 Characterization Results

Two samples were fabricated using the proposed technique. One sample has a thickness of 240 nm to measure the performance of the design, while the other has 600 nm to obtain the cross-sectional SEM image. The reflection spectra of the fabricated samples were acquired in the range Vis and NIR regions using a total reflection spectrophotometer which contains integrated sphere setup to account for the significant scattering effect we have observed due to disordered nanorods at the sample surface. The details of this characterization setup is given in the Experimental Section. Since there is no transmission in our design due to thick metallic bottom layer, measuring only the reflection is sufficient to determine the absorption inside the structure, by using the formula $A = 1 - R$. Measurement results demonstrate broadband absorption above 0.85 in Vis (from 0.3 μm to 0.78 μm) and above 0.75 in the whole NIR regime (from 0.78 μm to 2.5 μm) as shown in Figure 5.4(c). Optical properties of Bi provide a good impedance matching from air to the metal-air composite; and therefore, such a high absorption is attained in Vis. As explained in the theoretical section, Bi is the only metal whose effective permittivity in this design stays in the vicinity of ideal absorption region; however, it moves away from the ideal region with increasing wavelength. On the other hand, small gaps between densely packed metallic nanorods, see Figure 5.4(b), result in stronger localized field at longer wavelengths. The incident light is confined with high efficiency at the metal-air interface and between the small gaps in the NIR regime. The image of the fabricated small-area sample, from which all of the measurements are taken, is shown in the inset 1 of Figure 5.4(c). Inset 2 of the same figure shows a proof-of-concept 4-inch silicon wafer fabricated with the proposed method to demonstrate the large-scale compatibility.

The fabricated sample was characterized using FTIR technique in the MIR regime. The reflection spectra of the sample was measured from several different positions to attain an average response. As a result, a narrowband absorption centered on 6.54 μm was attained. To test sensing capability of the fabricated sample, poly(methyl methacrylate) (PMMA950K) was selected as the sensing

Table 5.1: Literature review and this work

Research	**Configuration**	**Sensitivity**
Liu et al. [45]	MIM nanodisc	400 nm/RIU
Liu et al. [107]	Planar metamaterial with cut-out structures in a thin gold film	588 nm/RIU
Lee et al. [110]	7x7 gold nanoslit array	668 nm/RIU
Di Meo et al. [111]	Cross-shaped plasmonic nanoantennas based chemical sensor	600 nm/RIU
Yong et al. [112]	MM based 4 cylindrical nanodiscs	885 nm/RIU
Pang et al. [113]	Nanohole array	1520 nm/RIU
Jin et al. [114]	Two cascaded micro-rings resonator	1300 nm/RIU
This work	**MM based randomly distributed/oriented Bi nanorods**	**2151 nm/RIU**

target because its complex refractive index has constant real part and zero imaginary part (i.e., zero absorption) in the range from 4 μm to 10 μm. 200 nm thick PMMA was spin coated on the randomly distributed Bi nanorods, and the resulting absorption response was characterized by using FTIR. Reflection spectra of bare and PMMA coated Bi nanorods are plotted in Figure 5.4(d). As it is seen from the figure, resonance wavelength is shifted from 6.54 μm to 7.59 μm in the amount of 1.05 μm due to PMMA. The sensitivity of the design is calculated as $S = 2151 nm/RIU$. The sensitivity of this design is significantly larger than the previously reported literature, as shown in Table 5.1. The ultra-high sensitive response of the structure to a change in refractive index arises from the fact that, in general, designs that set up strong interaction between sample and the resonant mode have high sensitivity [123]. As explained in the field confinement mechanism, the incident light is mainly coupled to the SPP modes excited at the Bi-air interface, and small gaps between metallic nanorods substantially improve the field localization at longer wavelengths. Tiny changes in the refractive index of the spacer material around nanorods naturally affect both the excited modes and interactions between metallic nanostructures. When a material with different refractive index (PMMA in this case) is replaced with air, modified nature of the coupling effects causes a red shift in the resonance. Thus, a refractive index sensing with ultra-high sensitivity is experimentally realized.

5.4 Experimentation Details

5.4.1 Fabrication of the Bismuth Nanorods

For the fabrication of the small-area samples, first, a typical commercial square-shaped Silicon substrate with 400 mm^2 area was cleaned with Acetone, Isopropanol, and deionized water, and then was dried with N_2 flow, to be used as a substrate. The surface was further treated using oxygen plasma for 5 minutes before starting the deposition of the films. Same procedure was followed for the 4-inch wafer. Firstly, 150 nm thick Bi back-reflector was coated by using a thermal evaporator system (MIDAS PVD 3T) at a chamber pressure of 3e-6 to 5e-6 torr and at a rate of 3 $\dot{A}$/s. Finally, the second layer with disordered and densely packed Bi nanorods was coated in the same equipment with the same parameters, but with the rate of 9 $\dot{A}$/s.

5.4.2 Optical Characterization

To measure the absorption spectra of the fabricated samples, reflectance in the mid-infrared range was measured over the range of 2.5 to 15 μm using an FTIR microscope with a numerical aperture of 0.4 (Bruker- Vertex 70v, Hyperion microscope). The instrument employs a mid-infrared source, KBr beamsplitter and nitrogen-cooled MCT-D313 detector. A 125 nm gold coated SiO_2/Si substrate was used as reference. Absorption of all the samples in the UV/VIS/NIR spectral ranges was obtained by measuring the reflection spectrum over the range from 300 nm to 2.5 μm. In these measurements, a commercial total reflection spectrophotometer (Agilent Cary 5000), utilizing a diffuse reflectance accessory (DRA) of a diameter of 110 mm was used. White polytetrafloroetilen (PTFE) was used as a reference.

5.4.3 Numerical Simulations

The designed structure was imitated as periodic, neatly packed cylindrical nanorods with high packing density. The bottom metallic layer was lied in the xy plane, and nanorods were elongated in the z-direction. A broadband plane-wave source, whose electric-field is polarized in the x-direction (i.e., TM polarization), was placed above the structure with a distance more than 4 μm. This source was impinged on the surface in the z-direction. It should be noted that polarization of the incident light does not have an influence on the absorption performance because the design is symmetric in all directions, and thus, it is polarization insensitive. Periodic boundary conditions were employed in the x- and y-directions while PML was adapted in the z-direction. Reflected and transmitted electromagnetic waves were collected using the power monitors at the top and bottom of the FDTD region. Absorption of the design can be calculated using the formula of $A = 1 - R - T$. Taking into consideration that the bottom layer is a thick metal coating, it behaves as a fully reflecting mirror and none of the light is transmitted through the design. Therefore, the aforementioned formula can be simplified as $A = 1 - R$.

Chapter 6

Conclusion

Properties of the perfect electromagnetic wave absorbers are determined by its two features, which are design configuration and constituent materials. While the design configuration (i.e., shape and geometry) can present new phenomena such as excitation of plasmonic waves, optical properties of the materials have a prominent importance on limits of the design. A creative design and wisely chosen materials remarkably improve the absorption spectrum bandwidth and strength.

In the first work, we demonstrated unprecedented potentials of transition metal carbides and nitrides to design perfect light absorbers in ultra-broadband range, and indicated that these materials perform perfect electromagnetic wave absorption in a larger bandwidth than metals in any configuration, owing to their excellent optical properties. Our numerical findings show that the proposed ceramic materials have wider bandwidth than all lossy and plasmonic materials in both planar metal-dielectric-metal-dielectric configuration and trapezoidal array of metal-dielectric pairs. In planar configuration, titanium carbide exhibits the largest bandwidth where an absorption above 0.9 is observed in the range of 405 nm-1495 nm. Using the trapezoidal array structure, the best performance is observed for vanadium nitride where an absorption above 0.9 is retained over

the range of 300 nm-2500 nm under TM polarization. In addition, we investigated the effects of possible fabrication inaccuracies in fabricating the trapezoidal array structure, and we proposed an alternative design to preserve the same performance. The superior absorption performance of transition metal carbides and nitrides over metals along with their higher durability against temperature, oxidation and erosion make them highly promising in ultra-broadband perfect absorber applications in which thermal requirements are strict in addition to high optical performance.

In the second work, we designed, fabricated and characterized a single metal, lithography-free, double functional device which has ultra-broadband absorption in the Vis and NIR spectral ranges, while narrowband absorption in the MIR regime. The proposed metal-metal design experimentally performs broadband absorption above 0.85 in Vis regime (0.3 μm-0.78 μm) and above 0.75 in the entire NIR regime (0.78 μm-2.5 μm) while it acts a narrowband absorber in the MIR range. The narrowband plasmonic resonance in the MIR range is utilized for refractive index sensing, and an ultra-high sensitivity of 2151 nm/RIU is experimentally obtained. We also numerically investigated our proposed device, by demonstrating the superior optical properties of Bi compared to other metals. In addition, utilization of oblique-angle deposition technique also allowed large-scale fabrication compatibility with high-throughput. Overall, utilizing the exceptional optical response of Bi in our large-scale compatible devices resulted in achieving double functionality with significant performances for each. The obtained results and findings reveal the unprecedented potential of Bi nanostructures for variety of applications including photo-conversion and sensing.

Bibliography

[1] D. R. Smith, J. B. Pendry, and M. C. Wiltshire, "Metamaterials and negative refractive index," *Science*, vol. 305, no. 5685, pp. 788–792, 2004.

[2] J. Yao, Z. Liu, Y. Liu, Y. Wang, C. Sun, G. Bartal, A. M. Stacy, and X. Zhang, "Optical negative refraction in bulk metamaterials of nanowires," *Science*, vol. 321, no. 5891, p. 930, 2008.

[3] A. J. Hoffman, L. Alekseyev, S. S. Howard, K. J. Franz, D. Wasserman, V. A. Podolskiy, E. E. Narimanov, D. L. Sivco, and C. Gmachl, "Negative refraction in semiconductor metamaterials," *Nature Materials*, vol. 6, no. 12, pp. 946–950, 2007.

[4] M. Lapine, I. V. Shadrivov, D. A. Powell, and Y. S. Kivshar, "Magnetoelastic metamaterials," *Nature Materials*, vol. 11, no. 1, pp. 30–33, 2012.

[5] G. T. Papadakis, D. Fleischman, A. Davoyan, P. Yeh, and H. A. Atwater, "Optical magnetism in planar metamaterial heterostructures," *Nature Communications*, vol. 9, no. 1, 2018.

[6] C. Menzel, C. Helgert, C. Rockstuhl, E. B. Kley, A. Tünnermann, T. Pertsch, and F. Lederer, "Asymmetric transmission of linearly polarized light at optical metamaterials," *Physical Review Letters*, vol. 104, no. 25, 2010.

[7] Z. Li, M. Mutlu, and E. Ozbay, "Chiral metamaterials: From optical activity and negative refractive index to asymmetric transmission," *Journal of Optics (United Kingdom)*, vol. 15, no. 2, 2013.

[8] A. Fang, T. Koschny, and C. M. Soukoulis, "Lasing in metamaterial nanostructures," *Journal of Optics A: Pure and Applied Optics*, vol. 12, no. 2, 2010.

[9] E. Plum, V. A. Fedotov, P. Kuo, D. P. Tsai, and N. I. Zheludev, "Towards the lasing spaser: controlling metamaterial optical response with semiconductor quantum dots," *Optics Express*, vol. 17, no. 10, p. 8548, 2009.

[10] D. Schurig, J. J. Mock, B. J. Justice, S. A. Cummer, J. B. Pendry, A. F. Starr, and D. R. Smith, "Metamaterial electromagnetic cloak at microwave frequencies," *Science*, vol. 314, no. 5801, pp. 977–980, 2006.

[11] J. Valentine, J. Li, T. Zentgraf, G. Bartal, and X. Zhang, "An optical cloak made of dielectrics," *Nature Materials*, vol. 8, no. 7, pp. 568–571, 2009.

[12] T. Ergin, N. Stenger, P. Brenner, J. B. Pendry, and M. Wegener, "Three-dimensional invisibility cloak at optical wavelengths," *Science*, vol. 328, no. 5976, pp. 337–339, 2010.

[13] N. I. Landy, S. Sajuyigbe, J. J. Mock, D. R. Smith, and W. J. Padilla, "Perfect metamaterial absorber," *Physical Review Letters*, vol. 100, no. 20, 2008.

[14] M. E. Stewart, C. R. Anderton, L. B. Thompson, J. Maria, S. K. Gray, J. A. Rogers, and R. G. Nuzzo, "Nanostructured plasmonic sensors," *Chemical Reviews*, vol. 108, no. 2, pp. 494–521, 2008.

[15] P. Offermans, M. C. Schaafsma, S. R. Rodriguez, Y. Zhang, M. Crego-Calama, S. H. Brongersma, and J. Gómez Rivas, "Universal scaling of the figure of merit of plasmonic sensors," *ACS Nano*, vol. 5, no. 6, pp. 5151–5157, 2011.

[16] T. Xu, Y. K. Wu, X. Luo, and L. J. Guo, "Plasmonic nanoresonators for high-resolution colour filtering and spectral imaging.," *Nature communications*, vol. 1, p. 59, 2010.

[17] N. I. Landy, C. M. Bingham, T. Tyler, N. Jokerst, D. R. Smith, and W. J. Padilla, "Design, theory, and measurement of a polarization-insensitive absorber for terahertz imaging," *Physical Review B - Condensed Matter and Materials Physics*, vol. 79, no. 12, 2009.

[18] A. Tittl, A. K. U. Michel, M. Schäferling, X. Yin, B. Gholipour, L. Cui, M. Wuttig, T. Taubner, F. Neubrech, and H. Giessen, "A Switchable Mid-Infrared Plasmonic Perfect Absorber with Multispectral Thermal Imaging Capability," *Advanced Materials*, vol. 27, no. 31, pp. 4597–4603, 2015.

[19] T. Ellenbogen, K. Seo, and K. B. Crozier, "Chromatic plasmonic polarizers for active visible color filtering and polarimetry," *Nano Letters*, vol. 12, no. 2, pp. 1026–1031, 2012.

[20] S. Yokogawa, S. P. Burgos, and H. A. Atwater, "Plasmonic color filters for CMOS image sensor applications," *Nano Letters*, vol. 12, no. 8, pp. 4349–4354, 2012.

[21] C. Ji, K. T. Lee, T. Xu, J. Zhou, H. J. Park, and L. J. Guo, "Engineering Light at the Nanoscale: Structural Color Filters and Broadband Perfect Absorbers," *Advanced Optical Materials*, vol. 5, no. 20, 2017.

[22] E. Rephaeli and S. Fan, "Absorber and emitter for solar thermo-photovoltaic systems to achieve efficiency exceeding the Shockley-Queisser limit," *Optics Express*, vol. 17, no. 17, p. 15145, 2009.

[23] J. K. Tong, W. C. Hsu, Y. Huang, S. V. Boriskina, and G. Chen, "Thin-film 'thermal well' emitters and absorbers for high-efficiency thermophotovoltaics," *Scientific Reports*, vol. 5, 2015.

[24] C. Wu, B. Neuner, J. John, A. Milder, B. Zollars, S. Savoy, and G. Shvets, "Metamaterial-based integrated plasmonic absorber/emitter for solar thermo-photovoltaic systems," *Journal of Optics*, vol. 14, no. 2, 2012.

[25] F. P. García De Arquer, A. Mihi, and G. Konstantatos, "Large-Area Plasmonic-Crystal-Hot-Electron-Based Photodetectors," *ACS Photonics*, vol. 2, no. 7, pp. 950–957, 2015.

[26] C. Hägglund and S. P. Apell, "Plasmonic near-field absorbers for ultrathin solar cells," *Journal of Physical Chemistry Letters*, vol. 3, no. 10, pp. 1275–1285, 2012.

[27] M. Entezari and M. Zavvari, "Application of Hyperbolic Metamaterials for Responsivity Enhancement of Thin Film Photo-Conductive Detectors," *IEEE Sensors Journal*, vol. 16, no. 24, pp. 8916–8920, 2016.

[28] W. Wang, A. Klots, D. Prasai, Y. Yang, K. I. Bolotin, and J. Valentine, "Hot Electron-Based Near-Infrared Photodetection Using Bilayer MoS2," *Nano Letters*, vol. 15, no. 11, pp. 7440–7444, 2015.

[29] V. E. Ferry, M. A. Verschuuren, H. B. T. Li, E. Verhagen, R. J. Walters, R. E. I. Schropp, H. A. Atwater, and A. Polman, "Light trapping in ultrathin plasmonic solar cells," *Optics Express*, vol. 18, no. S2, p. A237, 2010.

[30] O. Lopez-Sanchez, E. Alarcon Llado, V. Koman, A. Fontcuberta I Morral, A. Radenovic, and A. Kis, "Light generation and harvesting in a van der waals heterostructure," *ACS Nano*, vol. 8, no. 3, pp. 3042–3048, 2014.

[31] P. Spinelli, E. Ferry, J. Van De Groep, M. Van Lare, A. Verschuuren, I. Schropp, A. Atwater, A. Polman, P. Spinelli, V. E. Ferry, J. Van De Groep, M. Van Lare, M. A. Verschuuren, R. E. Schropp, H. A. Atwater, and A. Polman, "Plasmonic light trapping in thin-film Si solar cells," *Journal of Optics*, vol. 14, no. 2, 2012.

[32] Y. Wang, T. Sun, T. Paudel, Y. Zhang, Z. Ren, and K. Kempa, "Metamaterial-plasmonic absorber structure for high efficiency amorphous silicon solar cells," *Nano Letters*, vol. 12, no. 1, pp. 440–445, 2012.

[33] M. A. Green and S. Pillai, "Harnessing plasmonics for solar cells," *Nature Photonics*, vol. 6, no. 3, pp. 130–132, 2012.

[34] I. Massiot, N. Vandamme, N. Bardou, C. Dupuis, A. Lemaître, J. F. Guillemoles, and S. Collin, "Metal Nanogrid for Broadband Multiresonant Light-Harvesting in Ultrathin GaAs Layers," *ACS Photonics*, vol. 1, no. 9, pp. 878–884, 2014.

[35] C. F. Guo, T. Sun, F. Cao, Q. Liu, and Z. Ren, "Metallic nanostructures for light trapping in energy-harvesting devices," *Light: Science and Applications*, vol. 3, 2014.

[36] A. Ahmadivand, M. Karabiyik, and N. Pala, "Plasmonic photodetectors," in *Photodetectors: Materials, Devices and Applications*, pp. 157–193, Elsevier, 2015.

[37] T. G. U. Ghobadi, A. Ghobadi, E. Ozbay, and F. Karadas, "Strategies for Plasmonic Hot-Electron-Driven Photoelectrochemical Water Splitting," *ChemPhotoChem*, vol. 2, no. 3, pp. 161–182, 2018.

[38] W. Cai and V. Shalaev, *Optical metamaterials: Fundamentals and applications*. 2010.

[39] K. S. Yee, "Numerical Solution of Initial Boundary Value Problems Involving Maxwell's Equations in Isotropic Media," *IEEE Transactions on Antennas and Propagation*, vol. 14, no. 3, pp. 302–307, 1966.

[40] R. Doering and Y. Nishi, *Handbook of semiconductor manufacturing technology, second edition*. 2007.

[41] M. Razeghi and M. Razeghi, "Semiconductor Characterization Techniques," in *Fundamentals of Solid State Engineering* (M. Razeghi, ed.), pp. 597–621, Boston, MA: Springer US, 2019.

[42] P. Miao, L. F. Tam, and N. Xie, "Quasi-Local Mass Integrals and the Total Mass," *Journal of Geometric Analysis*, vol. 27, no. 2, pp. 1323–1354, 2017.

[43] Y. Li, L. Su, C. Shou, C. Yu, J. Deng, and Y. Fang, "Surface-enhanced molecular spectroscopy (SEMS) based on perfect-absorber metamaterials in the mid-infrared," *Scientific Reports*, vol. 3, 2013.

[44] W. Li and J. Valentine, "Metamaterial perfect absorber based hot electron photodetection," *Nano Letters*, vol. 14, no. 6, pp. 3510–3514, 2014.

[45] N. Liu, M. Mesch, T. Weiss, M. Hentschel, and H. Giessen, "Infrared perfect absorber and its application as plasmonic sensor," *Nano Letters*, vol. 10, no. 7, pp. 2342–2348, 2010.

[46] F. Ding, J. Dai, Y. Chen, J. Zhu, Y. Jin, and S. I. Bozhevolnyi, "Broadband near-infrared metamaterial absorbers utilizing highly lossy metals," *Scientific Reports*, vol. 6, 2016.

[47] J. Hendrickson, J. Guo, B. Zhang, W. Buchwald, and R. Soref, "Wideband perfect light absorber at midwave infrared using multiplexed metal structures," *Optics Letters*, vol. 37, no. 3, p. 371, 2012.

[48] P. Bouchon, C. Koechlin, F. Pardo, R. Haïdar, and J.-L. Pelouard, "Wideband omnidirectional infrared absorber with a patchwork of plasmonic nanoantennas," *Optics Letters*, vol. 37, no. 6, p. 1038, 2012.

[49] J. Hao, J. Wang, X. Liu, W. J. Padilla, L. Zhou, and M. Qiu, "High performance optical absorber based on a plasmonic metamaterial," *Applied Physics Letters*, vol. 96, no. 25, 2010.

[50] H. Wang and L. Wang, "Perfect selective metamaterial solar absorbers," *Optics Express*, vol. 21, no. S6, p. A1078, 2013.

[51] C. Wu and G. Shvets, "Design of metamaterial surfaces with broadband absorbance," *Optics Letters*, vol. 37, no. 3, p. 308, 2012.

[52] B. Zhang, J. Hendrickson, and J. Guo, "Multispectral near-perfect metamaterial absorbers using spatially multiplexed plasmon resonance metal square structures," *Journal of the Optical Society of America B*, vol. 30, no. 3, p. 656, 2013.

[53] A. Ghobadi, H. Hajian, B. Butun, and E. Ozbay, "Strong Light-Matter Interaction in Lithography-Free Planar Metamaterial Perfect Absorbers," *ACS Photonics*, vol. 5, no. 11, pp. 4203–4221, 2018.

[54] A. Ghobadi, H. Hajian, M. Gokbayrak, S. A. Dereshgi, A. Toprak, B. Butun, and E. Ozbay, "Visible light nearly perfect absorber: an optimum unit cell arrangement for near absolute polarization insensitivity," *Optics Express*, vol. 25, no. 22, p. 27624, 2017.

[55] K. Aydin, V. E. Ferry, R. M. Briggs, and H. A. Atwater, "Broadband polarization-independent resonant light absorption using ultrathin plasmonic super absorbers," *Nature Communications*, vol. 2, no. 1, 2011.

[56] J. Wang, Y. Chen, J. Hao, M. Yan, and M. Qiu, "Shape-dependent absorption characteristics of three-layered metamaterial absorbers at near-infrared," *Journal of Applied Physics*, vol. 109, no. 7, 2011.

[57] Q. Feng, M. Pu, C. Hu, and X. Luo, "Engineering the dispersion of metamaterial surface for broadband infrared absorption," *Optics Letters*, vol. 37, no. 11, p. 2133, 2012.

[58] Y. Zhang, L. Zhou, J. Q. Li, Q. J. Wang, and C. P. Huang, "Ultra-broadband and strongly enhanced diffraction with metasurfaces," *Scientific Reports*, vol. 5, 2015.

[59] W. Guo, Y. Liu, and T. Han, "Ultra-broadband infrared metasurface absorber: reply," *Optics Express*, vol. 27, no. 4, p. 5351, 2019.

[60] M. G. Nielsen, A. Pors, O. Albrektsen, and S. I. Bozhevolnyi, "Efficient absorption of visible radiation by gap plasmon resonators," *Optics Express*, vol. 20, no. 12, p. 13311, 2012.

[61] D. Hu, H.-Y. Wang, and Q.-F. Zhu, "Design of an ultra-broadband and polarization-insensitive solar absorber using a circular-shaped ring resonator," *Journal of Nanophotonics*, vol. 10, no. 2, p. 026021, 2016.

[62] S. Shen, W. Qiao, Y. Ye, Y. Zhou, and L. Chen, "Dielectric-based subwavelength metallic meanders for wide-angle band absorbers," *Optics Express*, vol. 23, no. 2, p. 963, 2015.

[63] N. Mattiucci, M. J. Bloemer, N. Aközbek, and G. D'aguanno, "Impedance matched thin metamaterials make metals absorbing," *Scientific Reports*, vol. 3, 2013.

[64] A. Ghobadi, S. A. Dereshgi, H. Hajian, G. Birant, B. Butun, A. Bek, and E. Ozbay, "97 percent light absorption in an ultrabroadband frequency range utilizing an ultrathin metal layer: Randomly oriented, densely packed

dielectric nanowires as an excellent light trapping scaffold," *Nanoscale*, vol. 9, no. 43, pp. 16652–16660, 2017.

[65] A. Ghobadi, S. A. Dereshgi, H. Hajian, B. Bozok, B. Butun, and E. Ozbay, "Ultra-broadband, wide angle absorber utilizing metal insulator multilayers stack with a multi-thickness metal surface texture," *Scientific Reports*, vol. 7, no. 1, 2017.

[66] S. Abedini Dereshgi, A. Ghobadi, H. Hajian, B. Butun, and E. Ozbay, "Ultra-Broadband, Lithography-Free, and Large-Scale Compatible Perfect Absorbers: The Optimum Choice of Metal layers in Metal-Insulator Multilayer Stacks," *Scientific Reports*, vol. 7, no. 1, 2017.

[67] J. G. Lei, B. Y. Ji, and J. Q. Lin, "A high-performance light absorber based on a metamaterial nanopyramid array," *Chinese Journal of Physics*, vol. 54, no. 6, pp. 940–946, 2016.

[68] Y. Cui, K. H. Fung, J. Xu, H. Ma, Y. Jin, S. He, and N. X. Fang, "Ultra-broadband light absorption by a sawtooth anisotropic metamaterial slab," *Nano Letters*, vol. 12, no. 3, pp. 1443–1447, 2012.

[69] Q. Liang, T. Wang, Z. Lu, Q. Sun, Y. Fu, and W. Yu, "Metamaterial-Based Two Dimensional Plasmonic Subwavelength Structures Offer the Broadest Waveband Light Harvesting," *Advanced Optical Materials*, vol. 1, no. 1, pp. 43–49, 2013.

[70] D. Ji, H. Song, X. Zeng, H. Hu, K. Liu, N. Zhang, and Q. Gan, "Broadband absorption engineering of hyperbolic metafilm patterns," *Scientific Reports*, vol. 4, 2014.

[71] S. He, F. Ding, L. Mo, and F. Bao, "Light absorber with an ultra-broad flat band based on multi-sized slow-wave hyperbolic metamaterial thin-films," *Progress in Electromagnetics Research*, vol. 147, no. May, pp. 69–79, 2014.

[72] F. Ding, Y. Jin, B. Li, H. Cheng, L. Mo, and S. He, "Ultrabroadband strong light absorption based on thin multilayered metamaterials," *Laser and Photonics Reviews*, vol. 8, no. 6, pp. 946–953, 2014.

[73] Y. K. Zhong, S. M. Fu, N. P. Ju, M. H. Tu, B. R. Chen, and A. Lin, "Fully Planarized Perfect Metamaterial Absorbers With No Photonic Nanostructures," *IEEE Photonics Journal*, vol. 8, no. 1, 2016.

[74] J. Wang, W. Zhang, M. Zhu, K. Yi, and J. Shao, "Broadband Perfect Absorber with Titanium Nitride Nano-disk Array," *Plasmonics*, vol. 10, no. 6, pp. 1473–1478, 2015.

[75] G. V. Naik, J. L. Schroeder, X. Ni, A. V. Kildishev, T. D. Sands, and A. Boltasseva, "Titanium nitride as a plasmonic material for visible and near-infrared wavelengths [erratum]," *Optical Materials Express*, vol. 3, no. 10, p. 1658, 2013.

[76] M. B. Cortie, J. Giddings, and A. Dowd, "Optical properties and plasmon resonances of titanium nitride nanostructures," *Nanotechnology*, vol. 21, no. 11, 2010.

[77] G. V. Naik, J. Kim, and A. Boltasseva, "Oxides and nitrides as alternative plasmonic materials in the optical range [Invited]," *Optical Materials Express*, vol. 1, no. 6, p. 1090, 2011.

[78] W. Li, U. Guler, N. Kinsey, G. V. Naik, A. Boltasseva, J. Guan, V. M. Shalaev, and A. V. Kildishev, "Refractory plasmonics with titanium nitride: Broadband," *Advanced Materials*, vol. 26, no. 47, pp. 7959–7965, 2014.

[79] F. Chen, Q. Li, M. Li, H. Long, Y. Yao, P. Sun, and J. Zhang, "Perfect absorber at visible frequencies using TiN-based refractory plasmonic metamaterials," *16th International Conference on Numerical Simulation of Optoelectronic Devices, NUSOD 2016*, pp. 111–112, 2016.

[80] H. Wang, Q. Chen, L. Wen, S. Song, X. Hu, and G. Xu, "Titanium-nitride-based integrated plasmonic absorber/emitter for solar thermophotovoltaic application," *Photonics Research*, vol. 3, no. 6, p. 329, 2015.

[81] K. Chaudhuri, M. Alhabeb, Z. Wang, V. M. Shalaev, Y. Gogotsi, and A. Boltasseva, "Highly Broadband Absorber Using Plasmonic Titanium Carbide (MXene)," *ACS Photonics*, vol. 5, no. 3, pp. 1115–1122, 2018.

[82] M. Alhabeb, K. Maleski, T. S. Mathis, A. Sarycheva, C. B. Hatter, S. Uzun, A. Levitt, and Y. Gogotsi, "Selective Etching of Silicon from Ti 3 SiC 2 (MAX) To Obtain 2D Titanium Carbide (MXene)," *Angewandte Chemie - International Edition*, vol. 57, no. 19, pp. 5444–5448, 2018.

[83] K. Hantanasirisakul and Y. Gogotsi, "Electronic and Optical Properties of 2D Transition Metal Carbides and Nitrides (MXenes)," *Advanced Materials*, vol. 30, no. 52, p. 1804779, 2018.

[84] K. Chaudhuri, A. Shaltout, D. Shah, U. Guler, A. Dutta, V. M. Shalaev, and A. Boltasseva, "Photonic Spin Hall Effect in Robust Phase Gradient Metasurfaces Utilizing Transition Metal Nitrides," *ACS Photonics*, vol. 6, no. 1, pp. 99–106, 2019.

[85] Z. Wang, D. Shah, K. Chaudhuri, A. Catellani, M. Alhabeb, H. Reddy, X. Meng, S. I. Azzam, N. Kinsey, A. V. Kildishev, Y. L. Kim, V. M. Shalaev, A. Calzolari, Y. Gogotsi, and A. Boltasseva, "Emerging materials for tailorable nanophotonic devices," in *2018 12th International Congress on Artificial Materials for Novel Wave Phenomena, METAMATERIALS 2018*, no. 001, pp. 58–60, IEEE, 2018.

[86] H. Deng, Z. Li, L. Stan, D. Rosenmann, D. Czaplewski, J. Gao, and X. Yang, "Broadband perfect absorber based on one ultrathin layer of refractory metal," *Optics Letters*, vol. 40, no. 11, p. 2592, 2015.

[87] J. Pfluger, J. Fink, W. Weber, K. P. Bohnen, and G. Crecelius, "Dielectric properties of TiCx, TiNx, VCx, and VNx from 1.5 to 40 eV determined by electron-energy-loss spectroscopy," *Physical Review B*, vol. 30, no. 3, pp. 1155–1163, 1984.

[88] J. Pfluger and J. Fink, "Determination of Optical Constants by High-Energy, Electron-Energy-Loss Spectroscopy (EELS)," in *Handbook of Optical Constants of Solids*, pp. 293–311, 1997.

[89] Q.-Y. Wen, Y.-S. Xie, H.-W. Zhang, Q.-H. Yang, Y.-X. Li, and Y.-L. Liu, "Transmission line model and fields analysis of metamaterial absorber in the terahertz band," *Optics Express*, vol. 17, no. 22, p. 20256, 2009.

[90] Y. Lu, W. Dong, Z. Chen, A. Pors, Z. Wang, and S. I. Bozhevolnyi, "Gap-plasmon based broadband absorbers for enhanced hot-electron and photocurrent generation," *Scientific Reports*, vol. 6, 2016.

[91] A. Ghobadi, H. Hajian, A. R. Rashed, B. Butun, and E. Ozbay, "Tuning the metal filling fraction in metal-insulator-metal ultra-broadband perfect absorbers to maximize the absorption bandwidth," *Photonics Research*, vol. 6, no. 3, p. 168, 2018.

[92] M. C. Soydan, A. Ghobadi, D. U. Yildirim, V. B. Erturk, and E. Ozbay, "All Ceramic-Based Metal-Free Ultra-broadband Perfect Absorber," *Plasmonics*, 2019.

[93] Y. Zhang, T. Wei, W. Dong, K. Zhang, Y. Sun, X. Chen, and N. Dai, "Vapor-deposited amorphous metamaterials as visible near-perfect absorbers with random non-prefabricated metal nanoparticles," *Scientific Reports*, vol. 4, 2014.

[94] A. Moreau, C. Ciracì, J. J. Mock, D. R. Smith, R. T. Hill, A. Chilkoti, Q. Wang, and B. J. Wiley, "Controlled-reflectance surfaces with film-coupled colloidal nanoantennas," *Nature*, vol. 492, no. 7427, pp. 86–89, 2012.

[95] Z. V. Vardeny, A. Nahata, and A. Agrawal, "Optics of photonic quasicrystals," *Nature Photonics*, vol. 7, no. 3, pp. 177–184, 2013.

[96] J. Bravo-Abad, A. I. Fernández-Domínguez, F. J. García-Vidal, and L. Martín-Moreno, "Theory of extraordinary transmission of light through quasiperiodic arrays of subwavelength holes," *Physical Review Letters*, vol. 99, no. 20, 2007.

[97] D. Pacifici, H. J. Lezec, L. A. Sweatlock, R. J. Walters, and H. A. Atwater, "Universal optical transmission features in periodic and quasiperiodic hole arrays," *Optics Express*, vol. 16, no. 12, p. 9222, 2008.

[98] L. Dal Negro and S. V. Boriskina, "Deterministic aperiodic nanostructures for photonics and plasmonics applications," *Laser and Photonics Reviews*, vol. 6, no. 2, pp. 178–218, 2012.

[99] D. S. Wiersma, "Disordered photonics," *Nature Photonics*, vol. 7, no. 3, pp. 188–196, 2013.

[100] D. U. Yildirim, A. Ghobadi, M. C. Soydan, O. Atesal, A. Toprak, M. D. Caliskan, and E. Ozbay, "Disordered and Densely Packed ITO Nanorods as an Excellent Lithography-Free Optical Solar Reflector Metasurface," *ACS Photonics*, vol. 6, no. 7, pp. 1812–1822, 2019.

[101] M. K. Hedayati, M. Javaherirahim, B. Mozooni, R. Abdelaziz, A. Tavassolizadeh, V. S. K. Chakravadhanula, V. Zaporojtchenko, T. Strunkus, F. Faupel, and M. Elbahri, "Design of a perfect black absorber at visible frequencies using plasmonic metamaterials," *Advanced Materials*, vol. 23, no. 45, pp. 5410–5414, 2011.

[102] M. K. Hedayati, F. Faupel, and M. Elbahri, "Tunable broadband plasmonic perfect absorber at visible frequency," *Applied Physics A: Materials Science and Processing*, vol. 109, no. 4, pp. 769–773, 2012.

[103] K. Bae, G. Kang, S. K. Cho, W. Park, K. Kim, and W. J. Padilla, "Flexible thin-film black gold membranes with ultrabroadband plasmonic nanofocusing for efficient solar vapour generation," *Nature Communications*, vol. 6, 2015.

[104] T. Stelzner, M. Pietsch, G. Andrä, F. Falk, E. Ose, and S. Christiansen, "Silicon nanowire-based solar cells," *Nanotechnology*, vol. 19, no. 29, 2008.

[105] H. Fang, X. Li, S. Song, Y. Xu, and J. Zhu, "Fabrication of slantingly-aligned silicon nanowire arrays for solar cell applications," *Nanotechnology*, vol. 19, no. 25, 2008.

[106] Y. J. Jen, Y. J. Huang, W. C. Liu, and Y. W. Lin, "Densely packed aluminum-silver nanohelices as an ultra-thin perfect light absorber," *Scientific Reports*, vol. 7, 2017.

[107] N. Liu, T. Weiss, M. Mesch, L. Langguth, U. Eigenthaler, M. Hirscher, C. Sönnichsen, and H. Giessen, "Planar metamaterial analogue of electromagnetically induced transparency for plasmonic sensing," *Nano Letters*, vol. 10, no. 4, pp. 1103–1107, 2010.

[108] D. U. Yildirim, A. Ghobadi, M. C. Soydan, M. Gokbayrak, A. Toprak, B. Butun, and E. Ozbay, "Colorimetric and Near-Absolute Polarization-Insensitive Refractive-Index Sensing in All-Dielectric Guided-Mode Resonance Based Metasurface," *The Journal of Physical Chemistry C*, vol. 123, pp. 19125–19134, jul 2019.

[109] D. U. Yildirim, A. Ghobadi, and E. Ozbay, "Near-absolute polarization insensitivity in grapheme based ultra-narrowband perfect visible light absorber," *Scientific Reports*, vol. 8, no. 1, 2018.

[110] K.-L. Lee, C.-W. Lee, W.-S. Wang, and P.-K. Wei, "Sensitive biosensor array using surface plasmon resonance on metallic nanoslits," *Journal of Biomedical Optics*, vol. 12, no. 4, pp. 044023–(1–5), 2007.

[111] V. Di Meo, A. Caporale, A. Crescitelli, M. Janneh, E. Palange, A. De Marcellis, M. Portaccio, M. Lepore, I. Rendina, M. Ruvo, and E. Esposito, "Metasurface based on cross-shaped plasmonic nanoantennas as chemical sensor for surface-enhanced infrared absorption spectroscopy," *Sensors and Actuators, B: Chemical*, vol. 286, pp. 600–607, 2019.

[112] Z. Yong, S. Zhang, C. Gong, and S. He, "Narrow band perfect absorber for maximum localized magnetic and electric field enhancement and sensing applications," *Scientific Reports*, vol. 6, 2016.

[113] L. Pang, G. M. Hwang, B. Slutsky, and Y. Fainman, "Spectral sensitivity of two-dimensional nanohole array surface plasmon polariton resonance sensor," *Applied Physics Letters*, vol. 91, no. 12, 2007.

[114] L. Jin, M. Li, and J. J. He, "Highly-sensitive silicon-on-insulator sensor based on two cascaded micro-ring resonators with vernier effect," *Optics Communications*, vol. 284, no. 1, pp. 156–159, 2011.

[115] J. Jágerská, H. Zhang, Z. Diao, N. L. Thomas, and R. Houdré, "Refractive index sensing with an air-slot photonic crystal nanocavity," *Optics Letters*, vol. 35, no. 15, p. 2523, 2010.

[116] K. V. Sreekanth, Y. Alapan, M. Elkabbash, E. Ilker, M. Hinczewski, U. A. Gurkan, A. De Luca, and G. Strangi, "Extreme sensitivity biosensing platform based on hyperbolic metamaterials," *Nature Materials*, vol. 15, no. 6, pp. 621–627, 2016.

[117] K. H. Yoon, M. L. Shuler, and S. J. Kim, "Design optimization of nanograting surface plasmon resonance sensors," *Optics Express*, vol. 14, no. 11, p. 4842, 2006.

[118] D. Ji, A. Cheney, N. Zhang, H. Song, J. Gao, X. Zeng, H. Hu, S. Jiang, Z. Yu, and Q. Gan, "Efficient Mid-Infrared Light Confinement within Sub-5-nm Gaps for Extreme Field Enhancement," *Advanced Optical Materials*, vol. 5, no. 17, 2017.

[119] A. Kubo, Y. S. Jung, H. K. Kim, and H. Petek, "Femtosecond microscopy of localized and propagating surface plasmons in silver gratings," *Journal of Physics B: Atomic, Molecular and Optical Physics*, vol. 40, no. 11, 2007.

[120] J. C. Yang, H. Gao, J. Y. Suh, W. Zhou, M. H. Lee, and T. W. Odom, "Enhanced optical transmission mediated by localized plasmons in anisotropic, three-dimensional nanohole arrays," *Nano Letters*, vol. 10, no. 8, pp. 3173–3178, 2010.

[121] Y. J. Shin, C. Pina-Hernandez, Y. K. Wu, J. G. Ok, and L. J. Guo, "Facile route of flexible wire grid polarizer fabrication by angled-evaporations of aluminum on two sidewalls of an imprinted nanograting," *Nanotechnology*, vol. 23, no. 34, 2012.

[122] S. Giudicatti, S. M. Marz, L. Soler, A. Madani, M. R. Jorgensen, S. Sanchez, and O. G. Schmidt, "Photoactive rolled-up TiO2 microtubes: Fabrication, characterization and applications," *Journal of Materials Chemistry C*, vol. 2, no. 29, pp. 5892–5901, 2014.

[123] I. M. White and X. Fan, "On the performance quantification of resonant refractive index sensors," *Optics Express*, vol. 16, no. 2, p. 1020, 2008.